PHYSICAL REVIEW D
PARTICLES AND FIELDS

THIRD SERIES, VOLUME 35, NUMBER 3 — 1 FEBRUARY 1987

Measurement of neutrino-proton and antineutrino-proton elastic scattering

L. A. Ahrens, S. H. Aronson, P. L. Connolly,* B. G. Gibbard, M. J. Murtagh,
S. J. Murtagh,† S. Terada,‡ and D. H. White§
Physics Department, Brookhaven National Laboratory, Upton, New York 11973

J. L. Callas, D. Cutts, J. S. Hoftun, M. Diwan, R. E. Lanou, and T. Shinkawa‡
Department of Physics, Brown University, Providence, Rhode Island 02912

Y. Kurihara
Department of Physics, Hiroshima University, Hiroshima, 730, Japan

K. Amako and S. Kabe
National Laboratory for High Energy Physics (KEK), Ibaraki-Ken 305, Japan

Y. Nagashima, Y. Suzuki, S. Tatsumi,** and Y. Yamaguchi
Physics Department, Osaka University, Toyanaka, Osaka 560, Japan

K. Abe,‡ E. W. Beier, D. C. Doughty,†† L. S. Durkin, S. M. Heagy, M. Hurley,‡‡
A. K. Mann, F. M. Newcomer, H. H. Williams, and T. York§§
Department of Physics, University of Pennsylvania, Philadelphia, Pennsylvania 19104

D. Hedin, M. D. Marx, and E. Stern
Department of Physics, State University of New York, Stony Brook, New York 11794

(Received 16 June 1986)

Measurements of the semileptonic weak-neutral-current reactions $\nu_\mu p \to \nu_\mu p$ and $\bar{\nu}_\mu p \to \bar{\nu}_\mu p$ are presented. The experiment was performed using a 170-metric-ton high-resolution target detector in the BNL wide-band neutrino beam. High-statistics samples yield the absolute differential cross sections $d\sigma(\nu_\mu p)/dQ^2$ and $d\sigma(\bar{\nu}_\mu p)/dQ^2$. A measurement of the axial-vector form factor $G_A(Q^2)$ is also presented. The results are in good agreement with the standard model $SU(2)\times U(1)$. The weak-neutral-current parameter $\sin^2\theta_W$ is determined to be $\sin^2\theta_W = 0.220 \pm 0.016(\text{stat})^{+0.023}_{-0.031}(\text{syst})$.

I. INTRODUCTION

During the past 12 years there have been a large number of experiments[1] on the weak neutral current which display the basic validity of the standard $SU(2)\times U(1)$ electroweak model.[2] With the direct discovery of the intermediate vector bosons[3] W and Z the standard model has been firmly established. It is natural to question whether $SU(2)\times U(1)$ represents the limit of the fundamental theory. Recent attempts at grand unification embed $SU(2)\times U(1)$ as the low-energy limit of a more complex theory.[4] Such theories generally predict "nonstandard" phenomena such as additional vector bosons, or additional Higgs particles. Consequently it remains of interest both to search for new phenomena and to make more precise measurements of known phenomena. In the latter category are measurements of $\sin^2\theta_W$ in all possible weak-neutral-current channels.

Apart from purely leptonic reactions, the simplest reactions, both experimentally and theoretically, with which to study weak neutral currents are the semileptonic elastic reactions:

$$\nu_\mu p \to \nu_\mu p \ , \tag{1.1}$$

$$\bar{\nu}_\mu p \to \bar{\nu}_\mu p \ . \tag{1.2}$$

The cross sections for these reactions are well known, within small theoretical uncertainty, and are largely independent of assumptions concerning the quark constituents of the proton. Radiative corrections to these cross sections are small (< 1%) (Ref. 5). Experimentally, reactions (1.1) and (1.2) provide a clean, distinctive signal. Reactions (1.1) and (1.2) are also so similar that by analyzing both reactions simultaneously, uncertainties in many experimental quantities correlate, which leads to reduced systematic errors on final results.

Neutrino-proton elastic scattering has played a significant role in our understanding of the weak neutral current. Neutrino-proton elastic scattering was measured in 1976 by the Columbia-Illinois-Rockefeller (CIR) (Ref. 6) and Harvard-Pennsylvania-Wisconsin (HPW) (Ref. 7) experiments at Brookhaven National Laboratory (BNL), and again in 1978 and 1980 at CERN (Refs. 8 and 9). Antineutrino-proton elastic scattering was also measured at BNL (Ref. 10). All experimental results prior to the experiment reported here are summarized in Ref. 11.

In this paper we present high-statistics measurements of the reactions $\nu_\mu p \to \nu_\mu p$ and $\bar{\nu}_\mu p \to \bar{\nu}_\mu p$. A brief report of the results in this paper has been presented previously.[12] The data were collected in an 170-metric-ton, high-resolution target-detector exposed to a horn-focused wide-band neutrino (antineutrino) beam from the alternating Gradient Synchrotron (AGS) at BNL. In Secs. I A and I B a brief description is given of neutrino-proton elastic-scattering kinematics and cross section phenomenology, respectively. The detector and neutrino beam are described in Sec. II. Section III explains the specifics of the $\nu_\mu p$ and $\bar{\nu}_\mu p$ signal extraction, background subtractions, and acceptance and efficiency corrections. Calculation of cross sections from the $\nu_\mu p$ and $\bar{\nu}_\mu p$ samples required measurement of the integrated neutrino fluxes on the detector. Since direct measurement of the neutrino flux is not possible, measurements of charged-current quasielastic scattering events $\nu_\mu n \to \mu^- p$ and $\bar{\nu}_\mu p \to \mu^+ n$ were made to determine this flux. Section IV provides details of this flux determination. In Sec. V a description is given of the systematic errors in the signal and normalization analyses. In Sec. VI the differential cross sections $d\sigma(\nu_\mu p)/dQ^2$ and $d\sigma(\bar{\nu}_\mu p)/dQ^2$ are displayed, and final results on $\sin^2\theta_W$ and the axial-vector form-factor $G_A(Q^2)$ are presented. The experiment yields the most accurate measurements of $d\sigma(\nu_\mu p)/dQ^2$ and $d\sigma(\bar{\nu}_\mu p)/dQ^2$ reported to date, and a precision measurement of $\sin^2\theta_W$, as well as a measurement of the axial-vector form factor.

A. Kinematics

Given the initial direction of the incident neutrino and a fixed proton target, a $\nu_\mu p$ elastic-scattering event is completely described by two independent kinematic variables. Possible choices include (θ_p, T_p), (E_ν, θ_p), or (E_ν, T_p), where T_p is the proton kinetic energy in the final state. The experimental quantities measured are the range of the scattered proton, its angle with respect to the direction of the incident neutrino θ_p and its rate of energy loss. Range and energy-loss measurements identify the particle as a proton, as opposed to a pion or muon, and determine its kinetic energy T_p. In the following analysis the data are presented in terms of the measured kinematic variables θ_p and Q^2, where

$$Q^2 = -q^2 = 2M_p T_p \ . \tag{1.3}$$

These measured quantities determine the neutrino energy through the kinematic relation

$$E_\nu = \frac{M_p}{\cos\theta_p (1 + 2M_p/T_p)^{1/2} - 1} \ . \tag{1.4}$$

In this experiment 80% of the neutrino-proton elastic scatters are from protons bound in carbon nuclei. In the kinematic regime of this experiment, the impulse approximation is valid; the protons in the carbon nucleus are taken to be free, except that the effects of Fermi momentum, the Pauli exclusion principle, and free particle nuclear scattering must be included in the analysis.

B. Phenomenology

Following the standard electroweak model, the effective Lagrangian for neutrino hadron elastic scattering is[13]

$$L^{\nu p} = -\frac{G_F}{\sqrt{2}} \bar{\nu} \gamma^\mu (1 + \gamma_5) \nu J^H_\mu \ . \tag{1.5}$$

A standard form for the hadronic current is

$$J^H_\mu = \alpha V^3_\mu + \beta A^3_\mu + \gamma V^0_\mu + \delta A^0_\mu + \cdots \ , \tag{1.6}$$

where the up- and down-quark contributions are combined to form V^2_μ (V^0_μ), the isovector (isoscalar) vector current, and A^3_μ (A^0_μ), the isovector (isoscalar) axial-vector current. The ellipses represent heavy-quark (s,c,b) terms. In the standard model,

$$\begin{aligned} \alpha &= 1 - 2\sin^2\theta_W \ , \\ \beta &= 1 \ , \\ \gamma &= -\tfrac{2}{3}\sin^2\theta_W \ , \\ \delta &= 0 \ , \end{aligned} \tag{1.7}$$

where the parameter $\sin^2\theta_W$ describes the strength with which the electromagnetic current mixes with the neutral component of the weak current. The vector currents are therefore the only ones containing $\sin^2\theta_W$.

Assuming time reversal invariance, the isospin invariance of the nucleon current, and the absence of second-class currents, the matrix element of J^H between nucleon states is given by

$$\langle f \,|\, J^H_\mu \,|\, i \rangle = \bar{u}_f(p') \left[\gamma_\mu F_1(Q^2) + i \frac{\sigma^{\mu\nu}}{2M_p} q^\nu F_2(Q^2) + \gamma_\mu \gamma_5 G_A(Q^2) \right] u_i(p) \ , \tag{1.8}$$

where q^ν is the momentum transfer, $u_i(p)$ and $\bar{u}_f(p')$ are initial and final nucleon wave functions, and F_1, F_2, and G_A are nucleon form factors which are real dimensionless functions of $Q^2 = -q^2$.

The vector form factors F_1 and F_2 are equated with empirical electromagnetic form factors obtained from electron-hadron scattering[14] in which the isovector and isoscalar form factors have the same Q^2 dependence. In addition it is assumed that the isovector and isoscalar vector form factors have the same Q^2 dependence in neutrino-proton scattering with

$$\begin{aligned} F_1+F_2&=\alpha G_V^3+\gamma G_V^0\ , \\ F_2&=\alpha F_V^3+\gamma F_V^0\ . \end{aligned} \tag{1.9}$$

In the dipole representation

$$\begin{aligned} G_V^3&=\frac{1}{2}\frac{(1+\kappa_p-\kappa_n)}{(1+Q^2/M_V{}^2)^2}\ , \\ G_V^0&=\frac{3}{2}\frac{(1+\kappa_p+\kappa_n)}{(1+Q^2/M_V{}^2)^2}\ , \\ F_V{}^3&=\frac{1}{2}\frac{(\kappa_p-\kappa_n)}{(1+\tau)(1+Q^2/M_V{}^2)^2}\ , \\ F_V^0&=\frac{3}{2}\frac{(\kappa_p+\kappa_n)}{(1+\tau)(1+Q^2/M_V{}^2)^2}\ , \\ \tau&=\frac{Q^2}{4M_p{}^2}\ , \end{aligned} \tag{1.10}$$

where $\kappa_p=1.793$ and $\kappa_n=-1.913$ are the anomalous magnetic moments of the proton and neutron, respectively, and $M_V=0.84$ GeV/c^2 is the vector dipole mass. Modifications of these form factors due to heavy-quark contributions are expected to be negligible.[15]

The axial-vector form factor

$$G_A(Q^2)=\beta G_A^3+\delta G_A^0 \tag{1.11}$$

is less well known. In the standard model, as mentioned above, δ is identically zero. In Sec. VI, however, this condition is relaxed when a search is made for additional contributions to the hadronic weak neutral current. In the dipole representation

$$G_A^3=\frac{1}{2}\frac{g_A(0)}{(1+Q^2/M_A{}^2)^2}\ , \tag{1.12}$$

where $g_A(0)=1.26$ is measured by neutron β decay. The value of the axial-vector dipole mass M_A has been measured in charged-current quasielastic neutrino reactions on an isoscalar target by three previous experiments.[16] An average value of M_A can be calculated from these experiments:

$$M_A=1.032\pm0.036 \text{ GeV}/c^2\ .$$

Heavy-quark contributions to $G_A(Q^2)$ are expected to be small but not negligible.[17] The Q^2 dependence of such corrections is not known. To avoid introducing more than one new parameter, additional contributions to $G_A(Q^2)$ have been searched for in this experiment by parametrizing $G_A(Q^2)$ as

$$G_A(Q^2)=\frac{1}{2}\frac{g_A(0)}{(1+Q^2/M_A{}^2)^2}(1+\eta) \tag{1.13}$$

and fitting for η. A nonzero value for η can be interpreted as due to either (1) heavy-quark contributions to the standard weak axial-vector current, or (2) a "nonstandard" primitive axial-vector isoscalar current.

Given the vector and axial-vector form factors the calculation of the differential cross section for $\nu p\rightarrow\nu p$ is straightforward, with the result

$$\frac{d\sigma}{dQ^2}=\frac{G_F^2M_p{}^2}{8\pi E_\nu^2}\left[A\pm B\frac{(s-u)}{M_p{}^2}+C\frac{(s-u)^2}{M_p{}^4}\right]\ , \tag{1.14}$$

where the plus sign is for neutrinos, the minus sign is for antineutrinos, and

$$\begin{aligned} s-u&=4M_pE_\nu-Q^2\ , \\ A&=\frac{Q^2}{M_p{}^2}\left[G_A^2\left[1+\frac{Q^2}{4M_p{}^2}\right]-F_1^2\left[1-\frac{Q^2}{4M_p{}^2}\right]\right. \\ &\qquad\left.+F_2^2\left[1-\frac{Q^2}{4M_p{}^2}\right]\frac{Q^2}{4M_p{}^2}+F_1F_2\frac{Q^2}{M_p{}^2}\right]\ , \end{aligned} \tag{1.15}$$

$$\begin{aligned} B&=\frac{Q^2}{M_p{}^2}G_A(F_1+F_2)\ , \\ C&=\frac{1}{4}\left[G_A^2+F_1^2+F_2^2\frac{Q^2}{4M_p{}^2}\right]\ . \end{aligned}$$

C. Radiative corrections

Radiative corrections to the theoretical elastic cross sections given in the preceding section are negligible (<0.5%) in the standard model. The only significant modification of theoretical formulas in this analysis from radiative corrections arise in the quasielastic cross sections needed for normalization. In this analysis both quasielastic cross sections have been multiplied by 1.02 to account for these corrections.[5]

II. THE EXPERIMENT

A. The detector

The experiment was performed using a 170-metric-ton high-resolution target-detector in a horn-focused neutrino (antineutrino) beam at the Brookhaven National Laboratory. The details of the detector have been given elsewhere[18] and are only briefly reiterated here.

The full detector is shown in Fig. 1. It consisted of three major sections: (i) a massive high-resolution modular target-detector; (ii) a shower counter for longitudinal containment of electron and photon showers; and (iii) a muon spectrometer, which was used to measure the energy spectra of both majority and minority ν_μ and $\bar{\nu}_\mu$ by measuring the angle and momentum of the muon produced in charged-current quasielastic interactions. The spatial coordinate system used in this report is a right-handed system with the positive z axis oriented in the beam direction (see Fig. 1). The positive y axis is in the upward vertical direction with the x,y origin centered in the detector.

The target detector was comprised of 112 modules, each of which contains a plane of 16 liquid-scintillator cells (each 4 m×25 cm×8 cm) and two crossed planes of 54 proportional drift tubes (PDT's) (each 4 m×7.6 cm

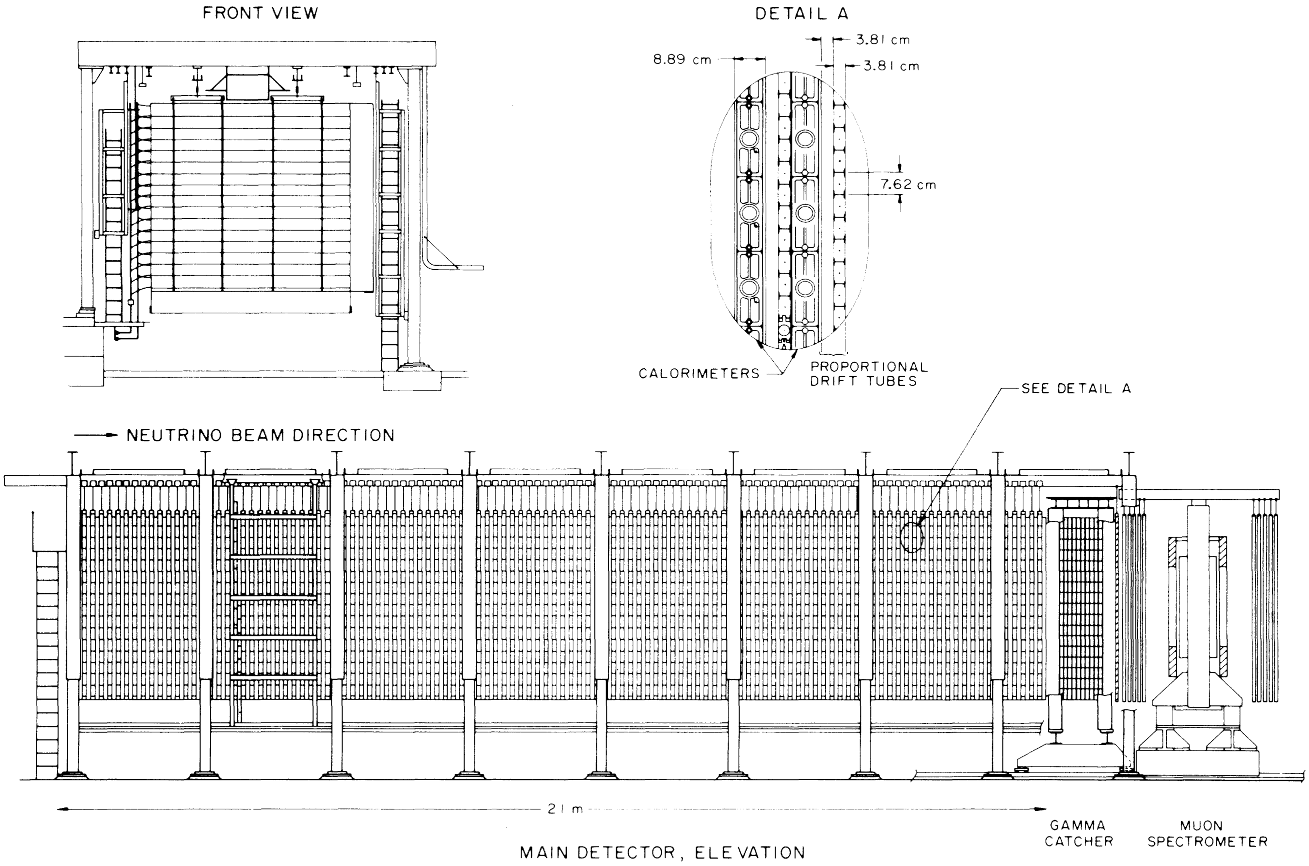

FIG. 1. A schematic drawing of the BNL—Brown—KEK—Osaka—Pennsylvania—Stony Brook neutrino detector.

×3.8 cm) arranged for x and y track position measurements. Each liquid-scintillator cell yielded charge (energy loss) and nsec-timing information while each PDT cell yielded charge and 1.5-mm-resolution position information. The fine segmentation (1892 scintillator cells and 12 096 PDT cells) and the pulse height and timing characteristics of the elements provided determination of event topology and discrimination of pions and protons through energy-loss measurements. 80% of the target-detector mass was liquid scintillator. 79% of the target protons were bound in carbon and aluminum while the remaining 21% were free protons.

The shower counter, located directly downstream of the main detector, consisted of 12 radiation lengths of lead and liquid-scintillation counters used to contain and measure electromagnetic energy from neutrino interactions occurring in the downstream part of the target detector. The shower counter was unnecessary in the analysis of neutrino-proton elastic scattering. The muon spectrometer was located downstream from the shower counter. It consisted of a wide aperture dipole magnet instrumented with nine x-y PDT plane pairs to measure the momenta of forward-going muons from ν_μ-induced quasielastic interactions. The detector was operated in a triggerless mode recording all information within a 10-μsec gate beginning at the AGS proton beam extraction and continuing several muon decay lifetimes after the passage of the neutrino beam.

Hardware failures were monitored and flagged on an event-by-event basis during the data taking and these spills were removed from the data samples. Off-line studies were made of the performance of detector elements to ensure run-by-run consistency of the data. Runs with major detector faults were removed from the samples. The percentage of events removed was less than 10%, and no biases were found in events removed from the samples.

B. The beam

The horn-focused wide-band neutrino beam[19] consisted of protons of 28-GeV kinetic energy incident on a production target producing pions and kaons which subsequently decayed yielding primarily ν_μ (positive horn focus) or $\bar{\nu}_\mu$ (negative horn focus) beams with mean energy 1.3 and 1.2 GeV, respectively. The ν_μ and $\bar{\nu}_\mu$ fluxes as a function of neutrino energy are shown in Figs. 2 and 3. In addition to the selected primary helicity neutrinos in a given beam a small fraction of opposite helicity neutrinos are produced by the decay of defocused mesons. This "wrong helicity" contamination was measured using the muon spectrometer by observing the fraction of quasielastic events occur-

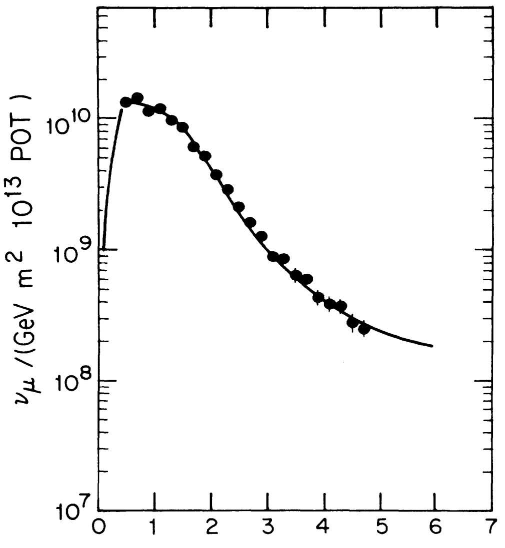

FIG. 2. The measured ν_μ flux. The error bars represent data from the reaction $\nu_\mu n \to \mu^- p$. The solid curve is a Monte Carlo beam flux calculation. Details of the flux measurement and Monte Carlo calculations are given in Ref. 19.

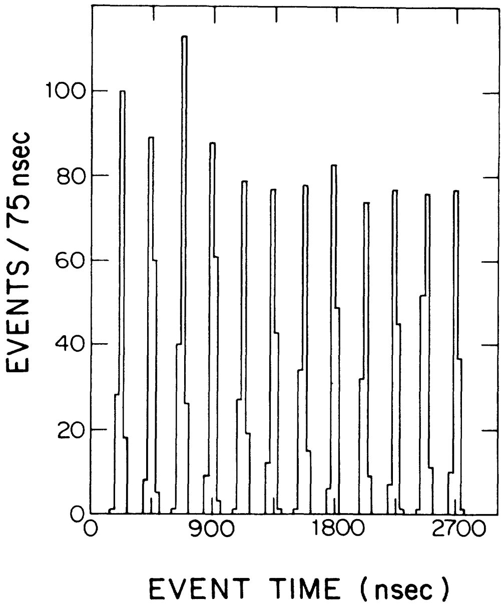

FIG. 4. The event time distribution of the neutrino-proton elastic-scattering sample relative to the start of the AGS beam spill showing the internal AGS time structure. The distribution for the antineutrino sample is similar.

ring with the wrong sign muon for the primary beam. The fraction (0–5 GeV) of antineutrino contamination in the neutrino beam was 0.024±0.005 while the neutrino contamination in the antineutrino beam was 0.087±0.013.

Relative to the standard transverse (x,y) coordinate system centered in the detector the beam axis coincided with the origin in the y direction and was offset by 0.5 m in the positive x direction. This offset is reflected in the slight asymmetry observed in the x vertex position distributions for events in the data samples.

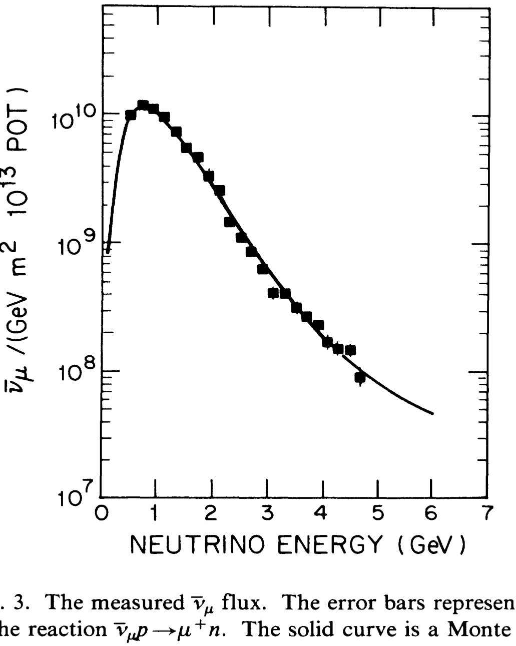

FIG. 3. The measured $\bar{\nu}_\mu$ flux. The error bars represent data from the reaction $\bar{\nu}_\mu p \to \mu^+ n$. The solid curve is a Monte Carlo beam flux calculation. Details of the flux measurement and Monte Carlo calculations are given in Ref. 19.

The neutrino beam preserves the internal AGS time (bunch) structure providing neutrinos in 12 distinct bunches of width 30 nsec spaced 224 nsec apart. Figure 4 shows a measurement of the time structure using actual neutrino interactions in the detector. Knowing the time of events relative to the AGS extraction and the given structure of the beam, "out-of-time" (background) events can be eliminated from the data.

III. SAMPLE EXTRACTION

A. Topological selection

Data were acquired in separate exposures of 0.55×10^{19} and 2.5×10^{19} protons on the AGS production target with the positive (ν_μ) and negative $(\bar{\nu}_\mu)$ focused beams, respectively. These exposures yielded 5.5×10^5 neutrino and 2.5×10^6 antineutrino recorded event bursts which comprised the data samples. The data were processed through a preliminary analysis program to convert the raw time and charge information for all struck elements with data into absolute time and energy depositions. To isolate scintillator element hits associated with individual interactions within the event gate (recall that there was no trigger) the preliminary analysis also localized groups of scintillator elements hits by time, i.e., time clusters. The typical window for a given time cluster was ~25 nsec, about the width of one AGS bunch (see Fig. 4). Therefore, if more than one interaction occurred per beam spill (not uncommon for neutrino running) there was only a one out of twelve chance of events overlapping in a given time cluster. Aside from random noise in individual detector elements, particles entering from outside the detector, or occasional overlapping events, this procedure clearly isolated scintillator element hits associated with individual neutrino interactions in the detector. Finally, PDT hits were associated with given time clusters and particle tracks were reconstructed from the PDT information.

After the events were reconstructed using the preliminary analysis a second pass was made to extract the final data sample. The first selection was based on the event topology. Initial cuts required event candidates to be fully contained single tracks with the interaction point inside the fiducial volume 2.0 m × 2.0 m × 86 modules. Since the minimum length for reconstructed tracks in the detector was three modules (three PDT plane pairs) observed protons were restricted to the region $Q^2 \geq 0.035$ (GeV/c)^2. In addition, to avoid confusion with other particle tracks, no additional reconstructed track was allowed in the same time cluster with a valid candidate track. This cut results in a random inefficiency associated primarily with particles entering the detector from the outside and the correction is discussed below in Sec. III F. These requirements excluded almost all charged-current interactions (most muons exit the detector), as well as a large fraction of inelastic neutral-current interactions with an energetic pion, or two or more charged particles in the final state (e.g., $\nu_\mu + n \rightarrow \nu_\mu + p + \pi^-$). Figure 5 shows a typical example of a candidate event selected by the above procedure.

B. Particle identification

The energy loss per segment along the tracks of candidate events was used to differentiate between protons and pions (muons). The fine-grained nature of the detector provided up to nine samples (three scintillator and six PDT) along the shortest tracks in the sample. The particle-identification (PID) procedure[20] compared the actual deposited energy in the ith cell (E^i_{meas}) along candidate tracks with that predicted for either a pion hypothesis or a proton hypothesis for the measured range. The most probable energy loss[21] (E^i_{pred}) was calculated for each element struck along the particle track for each hypothesis, taking into account the detailed detector geometry and composition. Separate likelihood functions were defined for scintillator data and PDT data for each of the two possible particle hypotheses:

$$\begin{aligned}
\ln[L^{\text{PDT}}(p)] &= \sum_i \ln[P_{\text{PDT}}(p, E^i_{\text{meas}}, E^i_{\text{pred}})] \,, \\
\ln[L^{\text{PDT}}(\pi)] &= \sum_i \ln[P_{\text{PDT}}(\pi, E^i_{\text{meas}}, E^i_{\text{pred}})] \,, \\
\ln[L^{\text{scin}}(p)] &= \sum_i \ln[P_{\text{scin}}(p, E^i_{\text{meas}}, E^i_{\text{pred}})] \,, \\
\ln[L^{\text{scin}}(\pi)] &= \sum_i \ln[P_{\text{scin}}(\pi, E^i_{\text{meas}}, E^i_{\text{pred}})] \,.
\end{aligned} \tag{3.1}$$

The functions $P(p(\pi), E^i_{\text{meas}}, E^i_{\text{pred}})$ represent the probability densities for a particle of given hypothesis and most likely energy deposition E^i_{pred}, yielding a measured energy E^i_{meas} in the ith element along a track. Measured shapes of deposited energy distributions in the detector elements were employed to determine the probability density functions P. Scintillator saturation effects were also included. To ensure valid energy-loss information criteria were established for both PDT and scintillator cells to eliminate elements containing visible particle interactions or information which was confused by crossing tracks from other time clusters. Cells failing these criteria were removed from the likelihood sums.

Finally, confidence levels (L_C) were evaluated for each hypothesis and both detector-element types using Monte Carlo integration of the likelihood functions from zero to the observed likelihood. The advantages of using these confidence levels to define the particle types were (i) when the probability densities are correctly calculated, the two distributions of confidence levels for the correct hypothesis are uniformly distributed between zero and one while those for the incorrect hypothesis are small, and (ii) the resulting distributions were insensitive to the number of energy-loss samples used.

Figures 6 and 7 show the confidence level for the pion

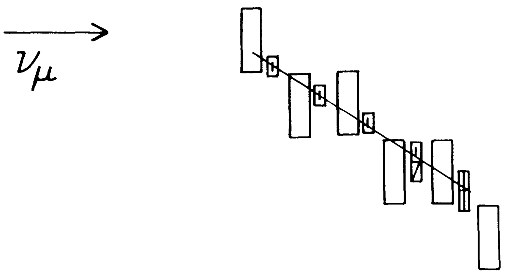

FIG. 5. The side view of a typical elastic-scattering candidate. The large boxes represent scintillator cells and the smaller boxes PDT cells hit. The best fit to the PDT drift positions (shown inside the PDT cells) is drawn on the event.

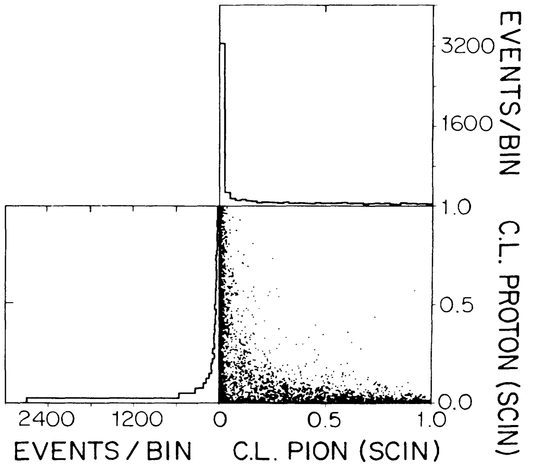

FIG. 6. Scatter plot for events passing the topological cuts of the confidence levels (C.L.'s) for a proton hypothesis vs a pion hypothesis using scintillator energy deposits.

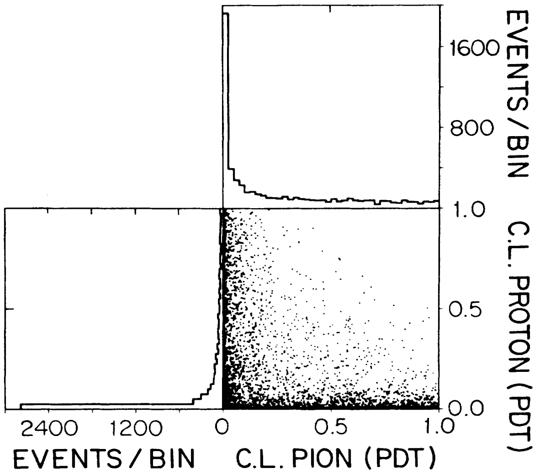

FIG. 7. Scatter plot for events passing the topological cuts of the confidence levels (C.L.'s) for a proton hypothesis vs a pion hypothesis using PDT energy deposits.

hypothesis plotted against the confidence level for the proton hypothesis for scintillator elements and PDT elements for events in the topologically cut sample. A clear separation between pion and proton events is evident in both plots. To maximize the separation efficiency both the PDT and scintillator information were used with the following criteria for a proton event:

$$\begin{aligned} &L_C^{\mathrm{PDT}}(p)>0.20 \text{ and } L_C^{\mathrm{scin}}(p)>0.05\ , \\ &L_C^{\mathrm{PDT}}(p)>0.05 \text{ and } L_C^{\mathrm{scin}}(p)>0.20\ , \\ &L_C^{\mathrm{PDT}}(\pi)<0.20 \text{ and } L_C^{\mathrm{scin}}(\pi)<0.20\ . \end{aligned} \tag{3.2}$$

The confidence levels for proton candidates as determined by scintillator and PDT data are shown in Fig. 8 along with the contour defined above. The distributions and projections are seen to be uniform, an indication that the probability distributions have been correctly modeled. After particle identification the data samples were reduced to 3015 $\nu_\mu p$ candidates and 2748 $\bar{\nu}_\mu p$ candidates.

Further evidence on the validity of the modeling was obtained from protons in a test beam incident on an apparatus of identical construction to the main detector.

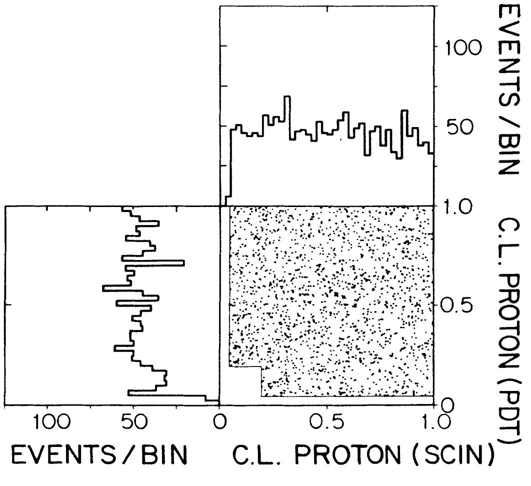

FIG. 8. Scatter plot for events passing the proton requirements and the topological cuts of the confidence levels (C.L.'s) for a proton hypothesis using PDT energy deposits vs a proton hypothesis using scintillator energy deposits to exhibit the uniformity of the distribution. The confidence-level boundary used to define protons (see Sec. III B) is indicated on the figure.

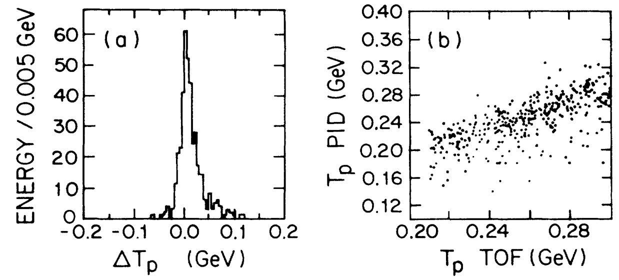

FIG. 9. (a) The proton kinetic energy measured by time of flight (TOF) in the test beam minus the reconstructed kinetic energy from the particle-identification procedure (PID). The slight asymmetry arises from Landau fluctuations. (b) A scatter plot of the measured proton kinetic energy (by time of flight) and the particle-identification reconstructed kinetic energy.

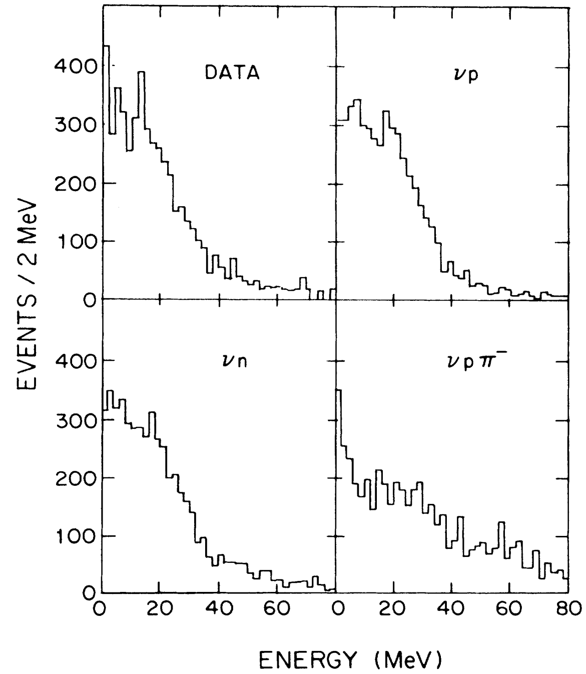

FIG. 10. Deposited energy distribution in the vertex (interaction) cell before energy cuts were applied for (a) the neutrino data sample, (b) Monte Carlo $\nu_\mu p$ events, (c) Monte Carlo $\nu_\mu n$ background events, and (d) Monte Carlo $\nu_\mu p \pi^-$ background events. This variable corresponds to that used in the first energy cut (1). These distributions have been scaled to a common total number of events.

The resulting confidence-level distributions for the proton hypothesis were found to be uniform for both PDT's and scintillator elements.

Since it was possible with the detector to observe the decay chain $\pi^+ \rightarrow \mu^+ \rightarrow e^+$, a check on pion rejection was made by looking for decay signatures at the end of tracks identified as protons. After corrections for the decay detection efficiency and spurious accidental decay signatures, the data showed that less than 1% of identified protons were misidentified pions.

The proton kinetic energy (T_p) was derived from a best-fit value provided by the particle-identification procedure and Q^2 was then calculated according to Eq. (1.3). The momentum of protons incident on the test beam detector was known most precisely from time of flight, this T_p was compared to the kinetic energy as derived from the PID procedure. Figure 9 shows the agreement between the two values of T_p.

C. Final selection

A combination of cuts based on the energy deposited at the proton track origin and surrounding regions was applied to eliminate events with additional charged particles emanating from the event vertex with a range too short to be tracked. These were (1) energy in the vertex (interaction) cell <50 MeV; (2) energy in a 5×5 scintillator cell

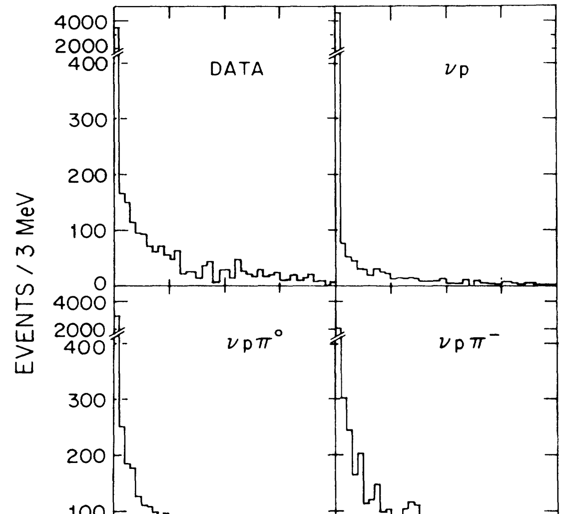

FIG. 11. Deposited energy distribution in a 5×5 scintillator cell region surrounding the interaction cell before energy cuts were applied for (a) the neutrino data sample, (b) Monte Carlo $\nu_\mu p$ events, (c) Monte Carlo $\nu_\mu p\pi^0$ background events, and (d) Monte Carlo $\nu_\mu p\pi^-$ background events. Energy depositions in cells associated with the candidate track are excluded. This variable corresponds to that used in the second energy cut (2). These distributions have been scaled to a common total number of events.

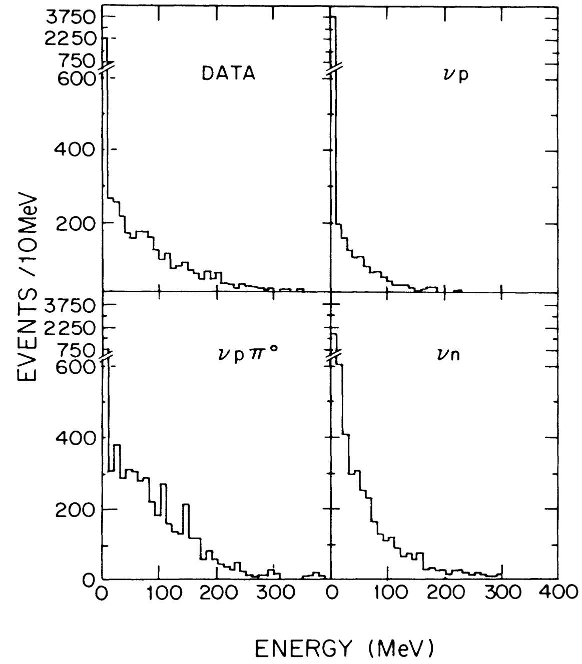

FIG. 12. Deposited energy distribution in a 5-m sphere surrounding the interaction cell before energy cuts were applied for (a) the neutrino data sample, (b) Monte Carlo $\nu_\mu p$ events, (c) Monte Carlo $\nu_\mu p\pi^0$ background events, and (d) Monte Carlo $\nu_\mu n$ background events. Energy depositions in cells associated with candidate track are excluded. This variable corresponds to that used in the third energy cut (3). These distributions have been scaled to a common total number of events.

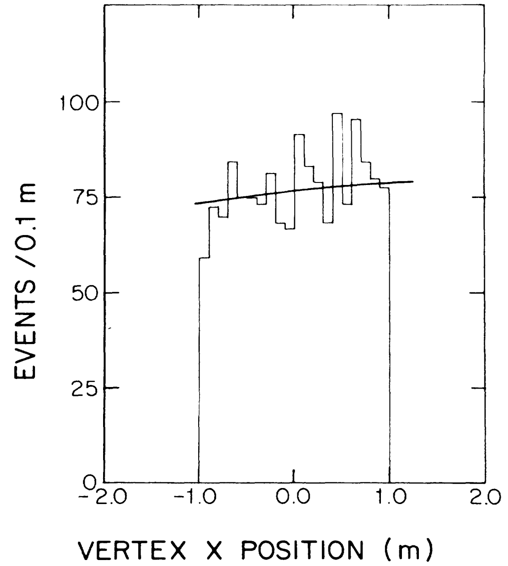

FIG. 13. The vertex x position relative to the center of the detector for the neutrino-proton elastic-scattering sample after all cuts. The histogram represents data events and the solid curve represents the Monte Carlo signal plus background prediction. The antineutrino-proton elastic-scattering distribution is similar.

TABLE I. Elastic-candidate analysis chain.

Analysis stage	Events remaining in the sample ν_μ	$\bar{\nu}_\mu$
Topological cuts: extra track, hardware failures, fiducial volume	18 835	18 855
Events passing PID	3 015	2 748
Energy cuts (final sample prior to background subtraction)	1 686	1 821

region surrounding the interaction point <30 MeV; (3) energy in a 5-m-radius sphere surrounding the interaction point <60 MeV. The third cut was designed primarily to remove neutral particles associated with the event (neutrons or gammas from π^0 decays). In calculating cuts (2) and (3) above, cells on the proton track were excluded. These cuts were chosen to maximize the background rejection while minimizing the uncertainty in modeling nuclear effects and neutral-particle detection efficiency in the Monte Carlo background calculations (see Sec. III D). Figures 10—12 show the energy distribution for the neutrino data, Monte Carlo signal, and selected Monte Carlo backgrounds for the three regions used for the cuts. These distributions for the antineutrino sample are similar. The final results were insensitive to reasonable variations of all three energy cuts.

These energy cuts reduced the samples to 1686 $\nu_\mu p$ candidates and 1821 $\bar{\nu}_\mu p$ candidates. Table I summarizes the number of events passing each stage in the event selection procedure. Figures 13—15 show the spatial distributions in x, y, and z of the interaction point for events in the final neutrino sample. The spatial distributions for the antineutrinos are similar. Figure 16 shows the angular distributions of events both before and after background subtraction (see Sec. III D). Finally, the interaction cell energy distributions are presented in Figs. 17 and 18.

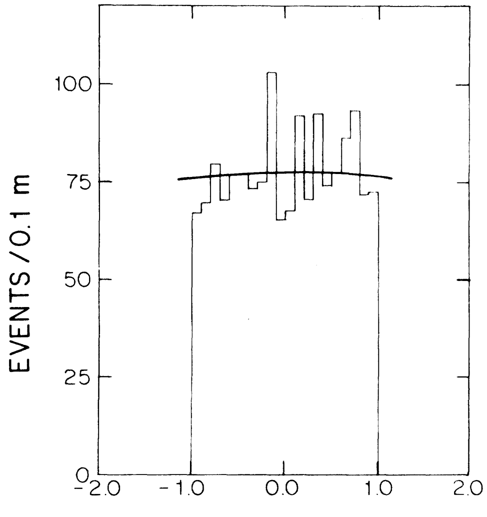

FIG. 14. The vertex y position relative to the center of the detector for the neutrino-proton elastic-scattering sample after all cuts. The histogram represents data events and the solid curve represents the Monte Carlo signal plus background prediction. The antineutrino-proton elastic-scattering distribution is similar.

D. Backgrounds

After all the analysis cuts some background events remained in the data samples. Backgrounds involving a muon or π^+ in the final state, which yielded observable decay signatures, were removed empirically. A potential background from neutrons entering from outside the detector was eliminated by restricting the fiducial region to approximately 19% of the total detector volume. The remaining backgrounds were calculated by Monte Carlo calculations (see the Appendix). These backgrounds arose from (i) charged-current neutrino interactions, (ii) neutrino-neutron elastic scattering where the final-state neutron scatters (including charge exchange) producing a visible proton in the detector, (iii) inelastic neutral-current interactions with single and multiple pion final states, and (iv) interactions of wrong-helicity neutrinos in the primary beam.

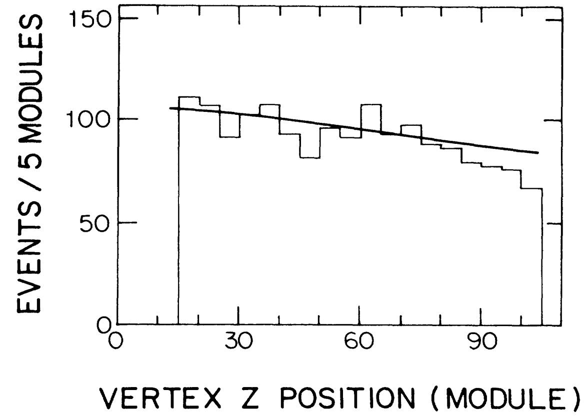

FIG. 15. The vertex z position relative to the front of the detector for the neutrino-proton elastic-scattering sample after all cuts. The histogram represents data events and the solid curve represents the Monte Carlo signal plus background prediction. The antineutrino-proton elastic-scattering distribution is similar.

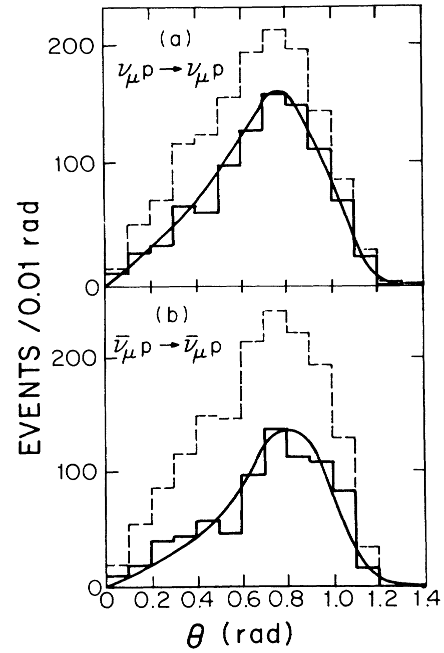

FIG. 16. Distributions in the angle θ_p of the proton candidates (a) $\nu_\mu p \rightarrow \nu_\mu p$, and (b) for $\bar{\nu}_\mu p \rightarrow \bar{\nu}_\mu p$. The dashed lines represent the data after PID and elimination of events with extra in-time energy depositions. The solid histograms are the observed elastic scattering signals after the Monte Carlo calculated background subtraction and the solid curves are the Monte Carlo calculated elastic-scattering distributions.

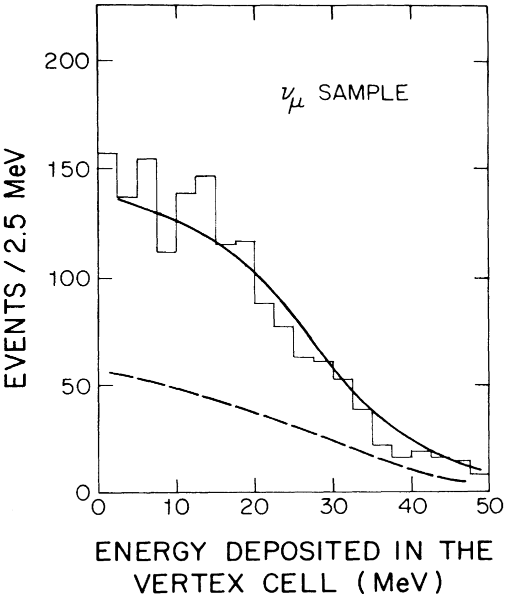

FIG. 17. The distribution of the energy deposited in the vertex (interaction) cell for the neutrino-proton elastic-scattering sample after all cuts. The histogram represents data events, the dashed curve the Monte Carlo background prediction, and the solid curve the Monte Carlo signal plus background prediction.

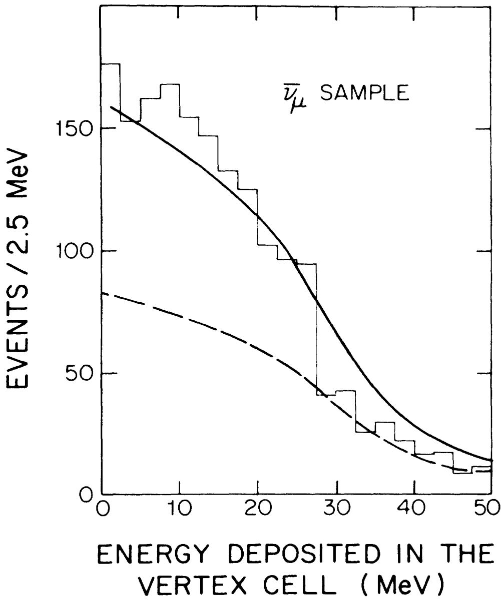

FIG. 18. The distribution of the energy deposited in the vertex (interaction) cell for the antineutrino-proton elastic-scattering sample after all cuts. The histogram represents data events, the dashed curve the Monte Carlo background prediction, and the solid curve the Monte Carlo signal plus background prediction.

Neutron interactions where the neutron enters from outside the detector volume contribution to the background through processes such as $np \rightarrow np$. Figure 4 shows the time of neutrino-proton elastic-scattering candidates relative to the beam gate. The bucket structure of the beam is clearly visible with virtually no event candidates occurring out of time with the beam. The distribution for the antineutrino sample is similar. This implies that if there are neutron-induced events in the detector the time coherence is maintained because the neutron source is from neutrino interactions just upstream of the detector rather than from neutrons produced by interactions of the primary proton beam upstream of the production target. To look for neutrons from nearby neutrino interactions entering the detector, the candidate event vertex distribution was examined. The longitudinal (z) vertex distribution, shown in Fig. 19, clearly indicates an enhancement near the front of the detector consistent with background from interactions of entering neutrons. The fiducial volume excluded the front of the detector in order to eliminate this background. The transverse vertex distributions showed only minor indications of neutron contamination and the transverse fiducial volume of 2 m$\times$2 m used for this experiment was chosen to render any background from entering neutrons negligible, as evidenced by the event vertex distributions predicted by Monte Carlo calculations in Figs. 13 and 14.

Charged-current events contributed to the background if the muon in the final state stopped close to the event vertex or otherwise escape direct detection. Detection of

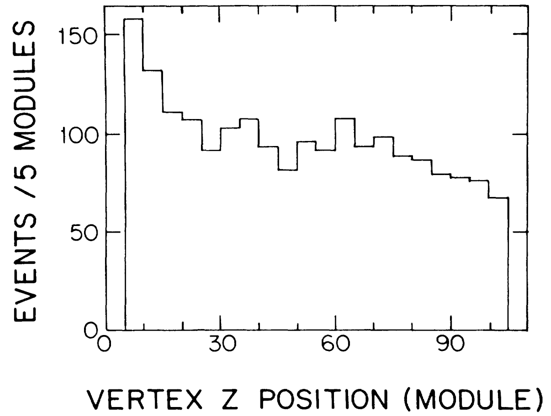

FIG. 19. The vertex z position of neutrino-proton elastic-scattering events with the upstream longitudinal fiducial volume relaxed to show the enhancement due to neutrons entering the front of the detector. The distribution for the antineutrino sample is similar.

the electron or positron from the decay of muons which stopped in the detector permitted the removal of charged-current contamination of this type, and also any neutral-current final state containing a stopping π^+. Negative pions preferentially capture in the detector and do not exhibit visible decay signatures. The measured detection efficiency for muon decay in the detector was 0.65 and corrections were made for the measured rate of accidental decay signatures. The residual background component not removed by the observation of decays (e.g., sideward-moving muons which escaped and did not satisfy the track-finding algorithm) was subtracted by Monte Carlo calculation. The backgrounds from decays are given in Table II.

The cross section for neutrinos interacting elastically with neutrons is comparable to that with protons and has similar dependence on $\sin^2\theta_W$ and M_A. For these events to mimic neutrino-proton elastic scatters the final-state neutron must produce a proton of sufficient energy to be accepted in the sample, thus reducing the number of such events. Nevertheless, the contribution from neutrino-neutron elastic scattering is a major component of the background comprising 16% of the final $\nu_\mu p$ sample and 11% of the final $\bar{\nu}_\mu p$ sample (see Table II). Since the visibility of these events depends on neutron scattering in the detector, checks were made to ensure that the Monte Carlo modeling of neutron scattering was correct. For example, antineutrino-induced quasielastic events ($\bar{\nu}_\mu p \to \mu^+ n$) were examined for interactions of the final-state neutron. These were compared in rate and character to the predictions of the Monte Carlo calculation and found to be in agreement. The treatment of systematic errors (see Sec. V) includes uncertainties associated with the modeling of neutron scattering.

Background events also came from single- (and multiple-) pion final-state neutral-current interactions in which the charged pions stopped without producing a visible track in the detector, or without sufficient visible energy to reject the event, and the neutral pions completely escaped detection. Included in these backgrounds are channels with a final-state neutron producing a proton in the same manner as in neutrino-neutron elastic scattering. Single-pion-inelastic processes were generated in the Monte Carlo calculation using the prescription of Rein and Seghal.[22] The total contributions of single-pion background channels to the final sample were 17% and 16% for the neutrino and antineutrino samples, respectively. Multiple-pion inelastic processes were modeled by Monte Carlo simulation using a combination of resonant and nonresonant production mechanisms with an overall scale set by measurements made in the seven-foot bubble chamber at BNL (Ref. 23). Multipion backgrounds comprised approximately 2.3% of the neutrino and antineutrino final samples.

Finally corrections were made for the wrong helicity contamination of each neutrino beam. The measured contamination of $\bar{\nu}_\mu$ in the ν_μ beam ($2.4\pm0.5\%$) coupled with the smaller cross section for $\bar{\nu}$ interactions compared to ν_μ interactions led to a negligible background contribution in the neutrino sample. However the larger contamination of ν_μ in the $\bar{\nu}_\mu$ beam ($8.7\pm1.3\%$) coupled with the larger

TABLE II. Evolution of the final elastic analysis data samples. (Numerical entries are the number of events observed or calculated.)

		Neutrino	Antineutrino
Elastic sample after PID and energy cuts		1686	1821
Decay subtraction	$\mu N, \nu N\pi^+$	146	160
Monte Carlo subtraction	$\nu N\pi$	283	297
	$\nu N\pi\pi$	38	41
	νn	268	196
Wrong-helicity beam contamination[a]		Negligible	351
Final elastic sample		951	776

[a] There is a measured $(8.7\pm1.3)\%$ contamination of ν_μ in the $\bar{\nu}_\mu$ beam, and a $(2.4\pm0.05)\%$ contamination of $\bar{\nu}_\mu$ in the ν_μ beam. These lead, for example, to ν_μ-induced events from $\nu p \to \nu p$, $\nu n \to \nu n$, and $\nu N \to \nu N\pi$ during data taking in the dominantly $\bar{\nu}_\mu$ beam. Corresponding contamination occurs in the quasielastic channels.

TABLE III. The fraction of observed events in each channel. These were calculated with $\sin^2\theta_W = 0.220$, $M_A = 1.032$ GeV/c^2, and $\eta = 0$. The fraction for events in the entire Q^2 range is listed.

ν_μ channel	Fraction	$\bar{\nu}_\mu$ channel	Fraction
$\nu_\mu p \to \nu_\mu p$(signal)	0.604	$\bar{\nu}_\mu p \to \bar{\nu}_\mu p$(signal)	0.482
$\nu_\mu n \to \nu_\mu n$	0.138	$\bar{\nu}_\mu n \to \bar{\nu}_\mu n$	0.089
$\nu_\mu p \to \nu_\mu p \pi^0$	0.038	$\bar{\nu}_\mu p \to \bar{\nu}_\mu p \pi^0$	0.039
$\nu_\mu n \to \nu_\mu p \pi^-$	0.041	$\bar{\nu}_\mu n \to \bar{\nu}_\mu p \pi^-$	0.039
$\nu_\mu p \to \nu_\mu n \pi^+$	0.015	$\bar{\nu}_\mu p \to \bar{\nu}_\mu n \pi^+$	0.016
$\nu_\mu n \to \nu_\mu n \pi^0$	0.007	$\bar{\nu}_\mu n \to \bar{\nu}_\mu n \pi^+$	0.012
$\nu_\mu n \to \mu^- p$	0.104		
$\bar{\nu}_\mu p \to \bar{\nu}_\mu p$ ($\bar{\nu}_\mu$ in ν_μ beam)	0.004	$\nu_\mu p \to \nu_\mu p$ (ν_μ in $\bar{\nu}_\mu$ beam)	0.125
		$\nu_\mu n \to \nu_\mu n$ (ν_μ in $\bar{\nu}_\mu$ beam)	0.029
Other $\bar{\nu}_\mu$ induced	0.003	Other ν_μ induced	0.056
Multipion	0.045	Multipion	0.113

neutrino cross sections, resulted in a 19% background from all ν_μ interactions. The primary effect of this contamination is to lessen the sensitivity of $\sin^2\theta_W$ to any simultaneous fit to the $\nu_\mu p$ and $\bar{\nu}_\mu p$ cross sections.

E. Background-subtraction tests

In order to check the consistency of our background calculation, an alternate analysis with redefined and tighter energy cuts was performed.[24] This analysis therefore has a higher background rejection than the standard analysis.

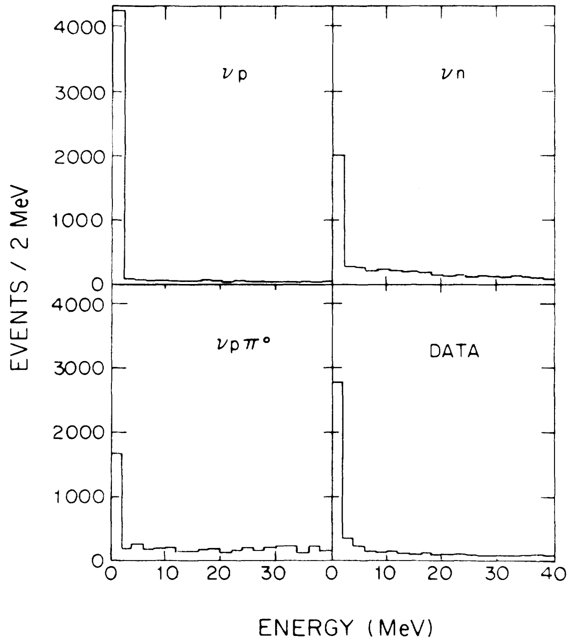

FIG. 20. Distribution of the redefined energy within a 5-m sphere (see Sec. III E) surrounding the interaction cell before energy cuts were applied for (a) Monte Carlo $\nu_\mu p$ events, (b) Monte Carlo $\nu_\mu n$ background events, (c) Monte Carlo $\nu_\mu p \pi^0$ background events, and (d) the neutrino data sample. These distributions have been scaled to a common total number of events.

The energy around the vertex was redefined to include the nine calorimeter cells surrounding the vertex cell including the cells on the proton track. The isolated energy was defined to include all cells within a 5-m radius of the vertex that were not on the track or in the nine-cell region. These cuts prove to be more sensitive to a particular class of background reactions.

Given this definition, the following cuts were applied: (i) energy in 9-cell region < 110 MeV, (ii) energy in the 5-m sphere < 20 MeV. These two replace cuts (2) and (3) in Sec. III C. The remainder of the selection requirements were identical. The largest difference between the two analyses is the redefined energy cut in the 5-m sphere. The distribution of this quantity is shown in Fig. 20.

Table III shows the background subtractions resulting from the use of the tighter cuts. The single-pion reactions have been reduced by a factor of about 2. The neutral-current $\nu_\mu n$ contamination has also been reduced.

The second analysis reduced the number of elastic proton events by about 5%. Almost all of these lost events had undergone a hard hadronic interaction. After all corrections, the results of this alternate analysis were within the statistical errors of the primary result.[25] Since this method decouples energy close to and away from the vertex, the cuts in this analysis depend differently on the backgrounds than the cuts in the primary analysis. The close agreement of the two methods therefore gives confidence that the Monte Carlo calculation is reproducing the contributing backgrounds correctly.

F. Acceptances and efficiencies

To calculate the absolute $\nu_\mu p$ and $\bar{\nu}_\mu p$ differential cross sections the observed distributions had to be corrected for various acceptance and efficiency losses. These factors were calculated using the Monte Carlo method described in the Appendix. Shown in Table IV are acceptance and efficiency factors for the $\nu_\mu p$ and $\bar{\nu}_\mu p$ samples averaged over the energy interval $0.2 < E_\nu < 5.0$ GeV and the Q^2 range $0.0 < Q^2 < Q_{\max}{}^2$. The errors listed are systematic. A variety of methods have been used to check these efficiencies.

The geometrical acceptance (first entry) in Table IV represents the percentage of $\nu_\mu p$ and $\bar{\nu}_\mu p$ events with a

TABLE IV. Elastic analysis acceptances and efficiencies.

	Neutrino	Antineutrino
Geometric acceptance	0.207	0.115
Extra-track-cut efficiency	0.81±0.02	0.90±0.01
Track-finding efficiency	0.86±0.03	0.91±0.03
Insufficient information	0.95±0.02	0.95±0.02
Confidence-level requirement on PID	0.75±0.03	0.77±0.03
Combined extra energy cuts	0.73±0.01	0.78±0.01

proton track at least 3 modules in length and fully contained within the detector. The difference between neutrino and antineutrino acceptances reflects the marked difference in Q^2 slope of the $\nu_\mu p$ and $\bar{\nu}_\mu p$ differential cross sections.

The extra track cut efficiency represents events removed from the sample by requiring only one track in a time cluster. These rejected events coincide in time with an unrelated interaction or a side entering muon. This fact has been estimated by the Monte Carlo calculation and by two other independent methods. Events which were selected as isolated proton tracks were scanned by eye to measure the fraction of events in which the time cluster contained an extra track. The average number of time clusters containing a track per AGS burst was also measured and the probability of two tracks in a single time cluster was calculated. These two methods gave similar extra track efficiency estimates. The difference between the neutrino and antineutrino values arose from the difference in beam intensity for the two data sets.

The track-finding efficiencies were found from eye scans of raw events entering the track-finding procedure, which resulted in tracking efficiencies ~4% lower than those calculated by the Monte Carlo method. The eye-scan efficiencies were used. The Q^2 and θ_p dependences of the tracking efficiency were also studied and found to be flat within statistics.

The efficiencies for the PID cuts were the results of a loss of events with insufficient information to permit particle identification (fourth entry) and a loss of events that fail the particle-identification criteria (fifth entry). The first category contains events in which the track was of minimal length and some energy information was missing making unambiguous particle identification impossible. Events in which the last scintillator on the track has invalid energy information were also excluded. These efficiencies were calculated from the known element efficiencies and also by scanning by eye the candidate events at the track level. There was good agreement between the different methods.

The efficiencies for events with sufficient PID information given in Table IV are lower than the PID geometric efficiency that would be calculated from Fig. 8. This extra loss is due to nuclear scattering of protons before they range out. These tracks do not fit a proton hypothesis and are rejected by the PID cuts. The PID efficiency was checked with test beam data as shown in Fig. 21, where the efficiency from the Monte Carlo calculation is plotted as a function of T_p. Also plotted is the test beam measurement of this efficiency. There is good agreement.

The energy cut efficiency (sixth entry) of Table IV represents the percentage of $\nu_\mu p$ and $\bar{\nu}_\mu p$ events removed from the sample by the various energy cuts. The events

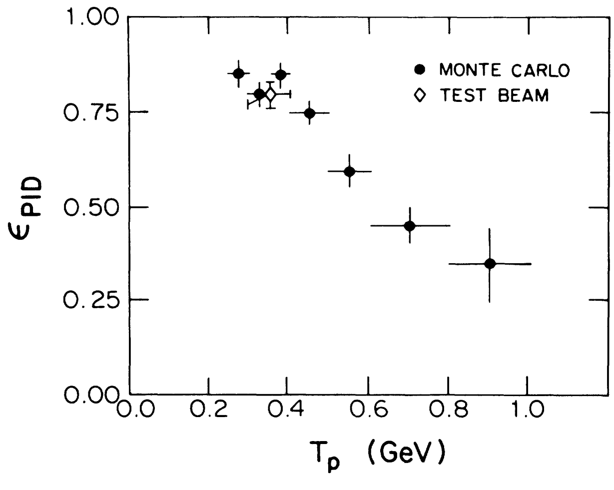

FIG. 21. The particle-identification efficiency as a function of proton kinetic energy as calculated by the Monte Carlo method. Also shown is the PID efficiency as measured for protons in the test beam apparatus.

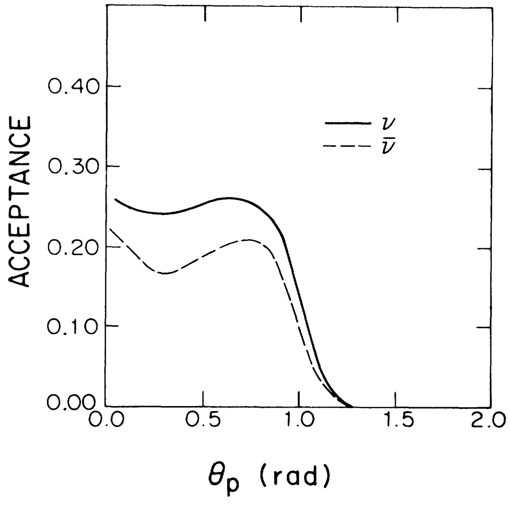

FIG. 22. The acceptance averaged over the beam spectra for neutrino- (antineutrino-) proton elastic scattering as a function of the proton angle θ_p.

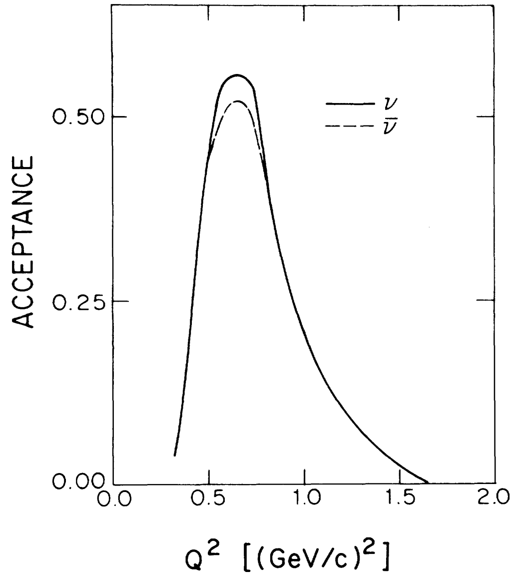

FIG. 23. The acceptance averaged over the beam spectra for neutrino- (antineutrino-) proton elastic scattering as a function of Q^2.

removed had energy not associated with the track due to secondary particles from the target nucleus or spurious noise hits. The modeling of the nuclear secondaries is discussed in the Appendix on the Monte Carlo simulator and the effect of the spurious noise hits are modeled by overlaying real data on Monte Carlo events. The small difference in $\nu_\mu p$ and $\bar{\nu}_\mu p$ samples comes from the differences in the neutrino flux.

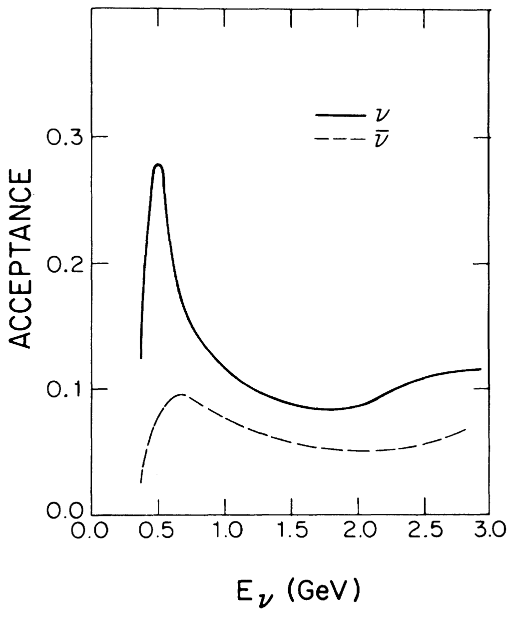

FIG. 24. The acceptance averaged over Q^2 for neutrino- (antineutrino-) proton elastic scattering as a function of the incident neutrino energy E_ν. Note that in the energy region below 0.5 GeV, where the acceptance is large and radically changing, the neutrino fluxes are falling rapidly. Hence, the observed events come predominantly from the neutrino energy region greater than 0.5 GeV where the changes in the acceptance as a function of energy are more moderate.

The event acceptance is shown in Figs. 22 and 23 as a function of θ_p and Q^2, respectively, which includes all the factors listed in Table IV. The θ_p dependence is simply explained. The acceptance is almost independent of angle at low θ_p, while at larger angles the proton length and containment criteria lower the acceptance. The Q^2 dependence is slightly more complex. The rise in acceptance in the region of $Q^2=0.25$ GeV$^2/c^2$ results from events gaining enough kinetic energy to pass the three-module length requirement. The falloff at higher Q^2 is due to lack of containment and secondary nuclear interactions. For completeness Fig. 24 displays the acceptance as a function of E_ν.

IV. NORMALIZATION

A. Introduction

Calculation of the cross section for $\nu_\mu p$ and $\bar{\nu}_\mu p$ elastic scattering requires knowledge of the total integrated neutrino flux incident on the detector in the fiducial volume defined for the elastic-scattering samples. Equivalently, the event rate for neutrino-proton elastic scattering can be compared to the event rate of a process of known cross section, which indirectly measures the integrated neutrino flux. In this experiment the total event rates of quasielastic scattering, $\nu_\mu n \to \mu^- p$ and $\bar{\nu}_\mu p \to \mu^+ n$, were measured to normalize the elastic scattering results to absolute cross sections. The quasielastic processes were chosen because of their simple topology and large contribution to the total cross section in the energy range of this experiment. In addition, the differential cross sections for quasielastic scattering are well understood theoretically and confirmed experimentally. They are similar in form to the neutrino-proton elastic-scattering cross sections but are independent of $\sin^2\theta_W$. Reference 26 gives these cross sections in detail.

B. Sample selection

The data samples from which quasielastic event candidates were chosen were identical to those from which the elastic-scattering candidates were selected. A topological selection was used to isolate muon candidates produced by charged-current interactions. Initially, single-track events with a minimum track length corresponding to a muon energy greater than 350 MeV (20 modules) were selected. The long-track length made the sample selection insensitive to additional tracks in the same time cluster, and such events were not rejected, as was necessary in the elastic sample. The long-track length also eliminated most charge pions from the sample since the scattering probability for pions above this energy is large. To further reduce the background the tracks were required to be within 20° of the beam direction, which restricted the average Q^2 for these events to ~0.2 (GeV/c)^2, well below the value required for reconstructable proton tracks. The interaction point was restricted to the same fiducial region as in the elastic-scattering analysis.

TABLE V. Quasielastic event analysis chain.

Analysis stage	Events remaining in the sample ν	$\bar{\nu}$
Single-track topology, hardware failures, fiducial volume	47 053	48 662
Length cut (20 modules minimum)	27 286	38203
θ_μ cut (20° maximum)	22 335	34 811
Tube cut (final sample prior to background subtraction)	20 102	32 936

After the event topology and angular limit were defined a small fraction of events in which a single track was reconstructed but which were clear showers or overlapping multiple-track events remained in the sample. These events were eliminated by examining the scintillator multiplicity and energy distributions away from the event vertex inside a spatial cylinder (tube cut) surrounding the reconstructed track. The average number of scintillators hit per module along the track was required to be small (typically one per module for a muon) and the average energy per module was required to be consistent with a muon, which led to the rejection of the unwanted topologies with minimal loss of signal events as shown in Table VII.

The spatial distributions in x, y, and z of the vertex of the 20 102 $\nu_\mu n \to \mu^- p$ candidate events in the neutrino sample after all cuts are shown in Figs. 25—27. The distributions for the 32 936 $\bar{\nu}_\mu p \to \mu^+ n$ candidate events in the antineutrino sample are similar. These distributions differ from those of the elastic-scattering candidates because the two reactions have different energy-dependent acceptances, and the spatial distribution of beam neutrinos at the detector depends on neutrino energy. This effect was predicted by the beam Monte Carlo method and confirmed by experiment.[19] Visual scans of the candidate events confirmed the existence of clean samples of events containing a single muon candidate. Table V summarizes the number of event candidates at various stages of the sample selection.

C. Backgrounds

The primary backgrounds to quasielastic scattering were single-pion inelastic charged-current interactions. Topological selection removed background channels exhibiting two (or more) visible charged tracks. The

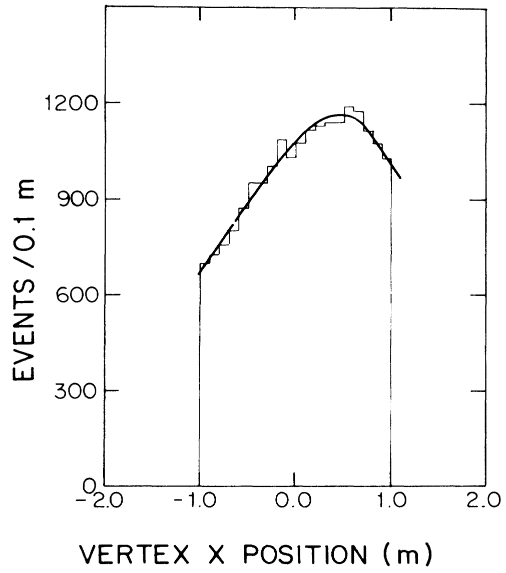

FIG. 25. The vertex x position relative to the center of the detector for the neutrino quasielastic-scattering sample after all cuts. The histogram represents data events and the solid curve represents the Monte Carlo signal plus background prediction. The antineutrino quasielastic-scattering distribution is similar.

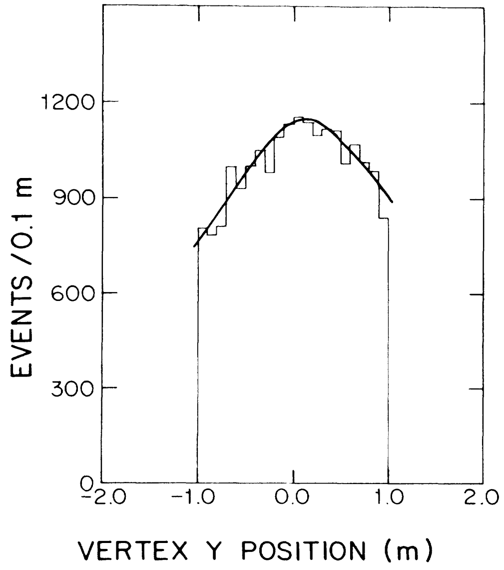

FIG. 26. The vertex y position relative to the center of the detector for the neutrino quasielastic-scattering sample after all cuts. The histogram represents data events and the solid curve represents the Monte Carlo signal plus background prediction. The antineutrino quasielastic-scattering distribution is similar.

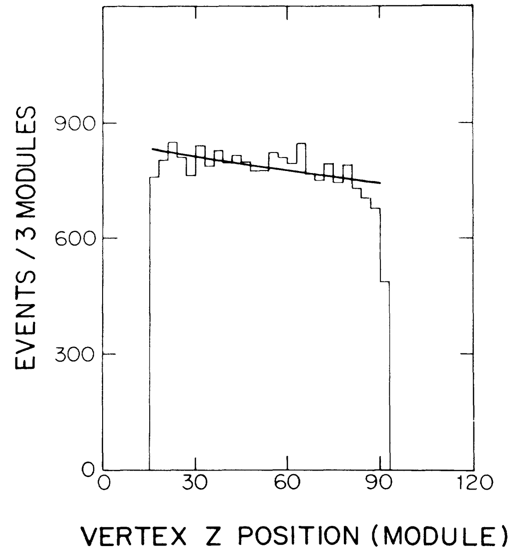

FIG. 27. The vertex z position relative to the front of the detector for the neutrino quasielastic-scattering sample after all cuts. The histogram represents data events and the solid curve represents the Monte Carlo signal plus background prediction. The antineutrino quasielastic-scattering distribution is similar.

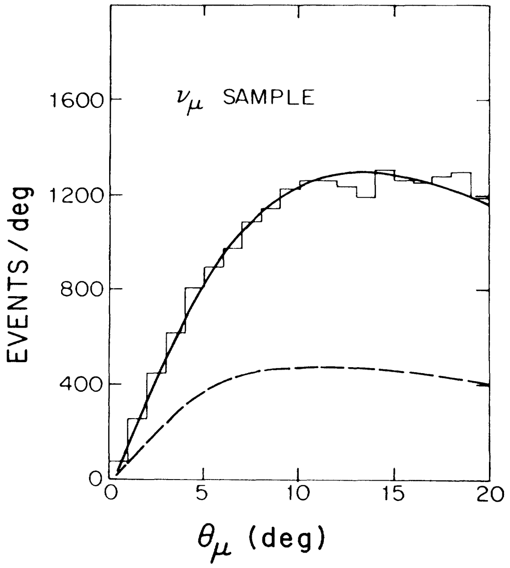

FIG. 28. The distribution of the muon angle θ_μ for the neutrino quasielastic sample after all cuts. The histogram represents data events, the dashed curve the Monte Carlo background prediction, and the solid curve the Monte Carlo signal plus background prediction.

remaining single-point and multipion backgrounds were calculated by the Monte Carlo method (see the Appendix). Table VI lists the relevant pion backgrounds which were subtracted from the candidate events samples.

The fraction of events in the two samples due to wrong-helicity neutrinos was calculated from the measured contaminations in the primary beams, taking into account all final states (quasielastics, single pion, etc.). The number of events subtracted are given in Table VI. The final background fractions from all contributions were 42% for the neutrino sample and 38% for the antineutrino sample.

A check of the charged-pion background calculation was made by observing pion decays near the event vertex in the neutrino sample. A statistical subtraction of events with decays (with appropriate accidental correction) was performed on both the data and Monte Carlo samples. The result agreed with the standard analysis in the total number of predicted quasielastic events to better than 3%. The single charged-pion backgrounds in the antineutrino sample contained a π^-, which was absorbed before it could decay, and consequently the decay signature was not used in the final data analysis to avoid an asymmetry in the treatment between the neutrino and antineutrino single-pion backgrounds.

D. Acceptances and efficiencies

The acceptance and efficiencies for the quasielastic samples are summarized in Table VII. They were determined by eye scan or by Monte Carlo calculation, and were averaged over the neutrino flux incident on the detector. The errors on these quantities are systematic.

The tracking efficiency was determined by eye scans of raw events entering the track-finding procedure and represents the ability of the event-reconstruction program to find muon tracks in the angular range of interest. The

TABLE VI. Evolution of the final quasielastic analysis data samples. (Numerical entries are the number of events observed or calculated.)

		Neutrino	Antineutrino
Quasielastic sample after angle and energy cuts		20 102	32 936
Monte Carlo subtraction	$\mu N\pi$	6945	7 888
	$\mu N\pi\pi$	776	879
Wrong-helicity beam contamination[a]		704	3 623
Final quasielastic sample		11 677	20 546

[a] See footnote in Table II.

TABLE VII. Quasielastic analysis acceptances and efficiencies.

	Neutrino	Antineutrino
Geometric acceptance	0.263	0.455
Tracking efficiency	0.85 ±0.02	0.86 ±0.01
Tube-cut efficiency	0.974±0.010	0.986±0.010

inefficiency was due to several effects including PDT inefficiency, multiple scattering, and noise from, e.g., crossing tracks.

The tube cut efficiency is dominated by noise effects. It was measured by overlapping random data on Monte Carlo quasielastic events.

E. Results

Figures 28 and 29 show the muon angle distributions for the ν_μ and $\bar{\nu}_\mu$ normalization data samples compared with the predicted muon angle distribution. Figures 30 and 31 show the energy deposited in the vertex cell in the normalization data samples compared with the Monte Carlo data and the excellent agreement is an indication of the correct modeling of the behavior of the secondary particles associated with the final states.

The fully corrected numbers of quasielastic events were calculated from the final background-subtracted samples given in Table VI with the efficiencies and acceptances given in Table VII. The results are 5.29×10^4 and 5.12×10^4 quasielastic events in the final neutrino and antineutrino samples, respectively.

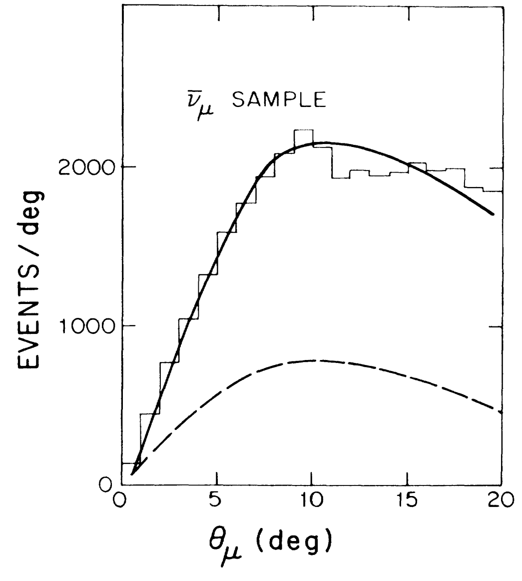

FIG. 29. The distribution of the muon angle θ_μ for the antineutrino quasielastic sample after all cuts. The histogram represents data events, the dashed curve the Monte Carlo background prediction, and the solid curve the Monte Carlo signal plus background prediction.

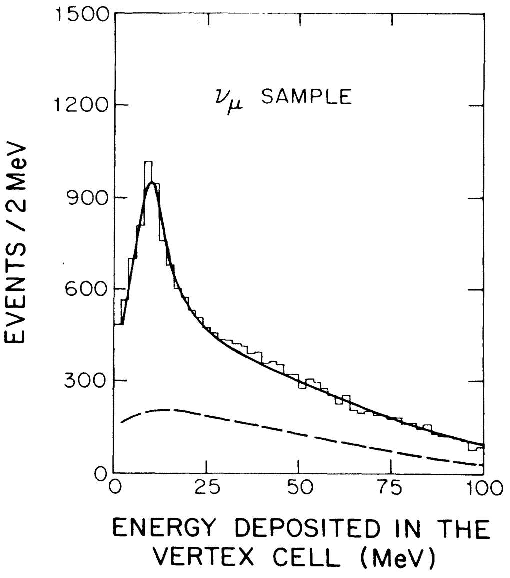

FIG. 30. The distribution of the energy deposited in the vertex (interaction) cell for the neutrino quasielastic sample after all cuts. The histogram represents data events, the dashed curve the Monte Carlo background prediction, and the solid curve the Monte Carlo signal plus background prediction.

Independent confirmation of the number of ν_μ-induced quasielastic events was obtained from quasielastic events in which both the muon and the proton tracks were visible in the detector. These fully reconstructed events yielded a total number of quasielastic neutrino events within 3% of that obtained from the single-prong topology data.

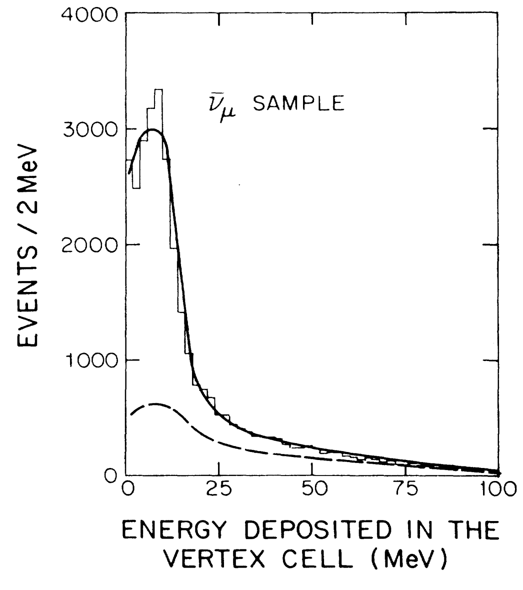

FIG. 31. The distribution of the energy deposited in the vertex (interaction) cell for the antineutrino quasielastic sample after all cuts. The histogram represents data events, the dashed curve the Monte Carlo background prediction, and the solid curve the Monte Carlo signal plus background prediction.

TABLE VIII. Q^2-independent systematic errors.

	σ_ν	$\sigma_{\bar{\nu}}$	$\sigma_{\nu\bar{\nu}}$
νp efficiencies			
Extra track cut	2.5%	1.1%	0%
Track finding	3.5%	3.3%	0%
Insufficient information	2.1%	2.2%	1%
PID	4%	4%	4%
Energy cuts	1.4%	1.3%	0%
Totals	6.4%	5.8%	4.1%
Quasielastic			
Track finding	2%	2%	1%
Tube cut	1%	1%	0%
Angle cut	2%	2%	1%
Totals	2.9%	3.0%	1.4%
Miscellaneous factors			
Energy scale	1%	1%	1%
Resolution	0%	0%	0%
Empirical background			
π-μ decay	1%	0.5%	0.5%
Noise	2%	2%	0%
Monte Carlo			
Nuclear effects	4%	4%	4%
π cross sections	3%	3%	3%
π scattering	2%	2%	2%
Isospin mix	1%	1%	1%
Pauli exclusion	2%	2%	2%
Fermi momentum	0%	1%	0%
Beam spectra shape	6%	3%	2%
Wrong helicity			
Beam contamination	0%	4%	0%
Totals	8.7%	8.1%	6.3%
Final total	11.2%	10.4%	7.6%

V. SYSTEMATIC ERRORS

Errors on the $\nu_\mu p \rightarrow \nu_\mu p$ and $\bar{\nu}_\mu p \rightarrow \bar{\nu}_\mu p$ cross sections were dominated by systematic uncertainties. These divide into Q^2-independent systematic errors (uncertainties affecting only the normalization scales) and Q^2-dependent systematic errors. They are discussed separately below. The correction for Q^2 resolution smearing is also described.

A. Q^2 independent systematics

Q^2 independent errors arise from uncertainties in corrections and subtractions applied to the signal and normalization samples. Many of the corrections to the event samples arise in a similar manner in the neutrino and antineutrino data sets, so their uncertainties are expected to be correlated. When a systematic error was assigned to the $\nu_\mu p$ and $\bar{\nu}_\mu p$ samples a correlation between the two was also estimated.

Shown in Table VIII is a list of the Q^2-independent systematic errors for the $\nu_\mu p$ and $\bar{\nu}_\mu p$ analysis. Uncertainties in $\nu_\mu p$ and $\bar{\nu}_\mu p$ selection efficiencies contributed 6.4% and 5.8% to the overall systematic errors, respectively. Track-finding and extra track cut efficiency systematics reflect the uncertainties (noise variation, efficiency variation, etc.) associated with eye scans of several hundred events each. Particle-identification systematics come from two sources. If a track contained invalid energy information in the last scintillator cell it was rejected. The systematic error in this factor reflects uncertainty in scintillator efficiencies. Additionally, a systematic error was assigned to the confidence level cuts. This error was estimated using test beam data as well as empirically determining the PID sensitivity to energy scale. Lastly, uncertainty in detector noise hits accounts for uncertainties in the energy cut efficiencies.

Uncertainties in the $\nu_\mu n \rightarrow \mu^- p$ and $\bar{\nu}_\mu p \rightarrow \mu^+ n$ normalization selection efficiencies contributed 2.9% and 3.0% to the overall systematic errors, respectively. The track-finding systematic error once again reflects uncertainties in eye scans of several hundred events each. Lastly, the tube cut error represents uncertainty in noise hits within the detector.

The last contribution to the Q^2-independent systematic error consisted of 8.7% (ν) and 8.1% ($\bar{\nu}$) from uncertainties in all of the miscellaneous factors listed in Table VIII. The systematic error associated with each of these factors was studied by modifying scattering models, cross sections, and Fermi momentum and Pauli exclusion corrections individually in the Monte Carlo and observing the effect on the normalization. In the interest of brevity, only the three largest effects are discussed here: nuclear interactions, single-pion backgrounds, and uncertainty of the neutrino beam energy spectrum.

To estimate systematic errors arising from nuclear scattering, charge exchange, and absorption within a carbon nucleus the nucleon cross sections in the Monte Carlo calculation were varied within their known errors ($\sim\pm 10\%$) (Ref. 27). Binding energy degradation of the primary proton leaving the nucleus could also effect the overall normalization and was varied within reasonable bounds.[28] Secondary particles from neutron or proton scattering within the carbon nucleus could deposit enough energy to cause rejection of a proton event. Events of the type $\nu_\mu n \to \mu^- p$ from the BNL seven-foot bubble chamber filled with neon[23] were compared with the Monte Carlo model, and a systematic error was assigned by comparing bubble chamber and Monte Carlo secondary particle energy distributions. Nuclear effects led to the systematic error of 4% in Table VIII, and were Q^2 independent within the Monte Carlo nuclear model. This systematic error is taken as fully correlated between neutrino and antineutrino data.

To estimate the normalization error due to uncertainties in single-pion cross sections (3% in Table VIII), these cross sections were varied in the Monte Carlo model. The variations were made simultaneously on backgrounds in both the signal and normalization samples. Single-pion production cross sections have been measured with limited statistics[29] and consequently the individual cross sections were varied by ±25%. The $I=\frac{1}{2}$ nonresonant production fraction was varied from zero to the value in the cross-section parametrization.[22] Pion absorption inside and outside the nucleus (a 2% contribution to Table III) was varied by ±30%. Correlations were calculated by observing simultaneous variation in $\nu_\mu p$ and $\bar{\nu}_\mu p$ results.

The neutrino energy spectra led to uncertainties of 6% and 3% in Table VIII. This sensitivity is attributed to the fact that the quasielastic normalization samples are produced by relatively-high-energy neutrinos [$E_\nu(\text{peak})\sim 2$ GeV] while the elastic signal samples came from low-energy neutrinos [$E_\nu(\text{peak})\sim 0.8$ GeV], which made the analysis sensitive to the relative neutrino flux in the two energy regions. The uncertainties in the $\phi_\nu(E_\nu)$ and $\phi_{\bar{\nu}}(E_\nu)$ measurements of Figs. 2 and 3 are due mostly to statistics with systematic contributions from background subtraction, Pauli exclusion, and M_A uncertainties. Propagating these uncertainties results in the systematic error given in Table VIII.

Adding in quadrature the errors of Table VIII yields a total systematic error of 11.2% for neutrinos and 10.4% for antineutrinos. The positive correlation coefficient between these systematic errors is

$$\rho=\sigma_{\nu\bar{\nu}}{}^2/\sigma_\nu\sigma_{\bar{\nu}}=\frac{(0.076)^2}{(0.112)(0.104)}=0.50\ . \tag{5.1}$$

B. Q^2-dependent systematics

A search was made for systematic shifts in the slope of the Q^2 distribution of events due to uncertainties in (1) proton kinetic-energy scale, (2) Fermi momentum, (3) Pauli exclusion, (4) energy resolution, (5) scattering within the target nucleus, (6) beam flux, (7) nuclear scattering outside the target nucleus, (8) particle identification, (9) vertex energy, (10) backgrounds, and (11) scintillator and PDT efficiencies. Only three effects influence the shape of the final Q^2 distribution appreciably: (1) scintillator and PDT efficiencies, (2) beam energy distributions, and (3) nuclear scattering outside the nucleus. These have been studied in detail by varying them in the Monte Carlo model. Table IX summarizes the Q^2-dependent systematic errors arising from these effects. Uncertainties in cell efficiencies arose from variations over time as well as uncertainty in the correlation between energy deposit and cell efficiency. These effects led to the largest Q^2-dependent systematic error as is shown in Table IX. Beam spectra uncertainties (see Ref. 19) also yielded a small Q^2 shape variation. Uncertainty in nuclear scattering cross sections of ±10% yielded small systematic errors except at the highest Q^2. These three effects are expected to be uncorrelated so that the final Q^2-dependent errors were calculated taking a quadrature sum.

The best check on the Q^2-dependent systematics errors was obtained by analyzing $\nu_\mu n \to \mu^- p$ events in which both the proton and the muon were tracked. The selection criteria for this sample were identical to the

TABLE IX. Q^2-dependent uncertainties.

	Cause					
			Beam spectra		Total	
Q^2	Scintillator and PDT inefficiency	Nuclear scattering	ν	$\bar{\nu}$	ν	$\bar{\nu}$
0.45	15%		4%	10%	15%	18%
0.55	8%		2%	3%	8%	8%
0.65	3%				3%	3%
0.75		2%			2%	2%
0.85		3%			3%	3%
0.95		4%			4%	4%
1.05		6%			6%	6%

$\nu_\mu p \rightarrow \nu_\mu p$ selection criteria with the addition of requiring (1) a two-prong event with a μ^- leaving the detector, and (2) an opening angle of $\theta_{\mu p} > 0.20$ rad between the proton and muon. After subtraction for decays near the event vertex, the remaining backgrounds were $\sim 9\%$. Shown in Fig. 32 is the Q^2 distribution measured for this sample. Overlaid on this distribution is the result expected from the theoretical cross section with $M_A = 1.032$ GeV/c^2. The agreement between the data and theoretical prediction is good. Except for possible errors due to the additional criteria (1) and (2) above, the systematic errors in the νp and $\nu_\mu n \rightarrow \mu^- p$ samples are nearly identical. Hence Fig. 32 places a strong constraint on the Q^2 shape uncertainty.

C. Q^2 resolution

The two kinematic variables θ_p and Q^2 measured in the $\nu_\mu p$ and $\bar{\nu}_\mu p$ analyses were smeared by: (1) energy resolution, (2) angular resolution, (3) nuclear scattering inside and outside the nucleus, (4) Fermi momentum, and (5) nuclear binding energy. Since the final cross sections were integrated over θ_p the analyses were insensitive to resolution effects in this variable. The Q^2 resolution smearing is approximately $0.1(\text{GeV}/c)^2$, due mainly to Fermi momentum in the target nuclei. To study the sensitivity of the final differential cross sections to resolution effects, three independent methods have been used.

The shapes of the final differential cross sections were shown to be insensitive to the resolution effects in the Monte Carlo calculation shown in Fig. 33 is a plot of $d\sigma/dQ^2$ calculated for $\nu_\mu p$ elastic scattering before and after including Fermi momentum in a simple Monte Carlo. The overall scale for the smeared plot was shifted by 3%. It is seen that the slope remained unchanged.

Additionally the final differential cross sections were checked by unfolding the Q^2 resolution smearing in the Monte Carlo calculation by binned-matrix techniques. The deconvoluted answer agreed with a simple bin-by-bin acceptance correction well within statistics as is shown in Fig. 34. The data point at $Q^2 = 0.35$ $(\text{GeV}/c)^2$ has been included in this plot to illustrate the large statistical errors associated with this region of Q^2. This point was not used in the analysis due to the statistical error, as well as the large systematic error associated with this point arising from uncertainties in the detector element efficiencies (see Sec. V B) and from uncertainties associated with the boundary conditions imposed for the deconvolution. The bin-by-bin acceptance correction was chosen to calculate the final differential cross sections.

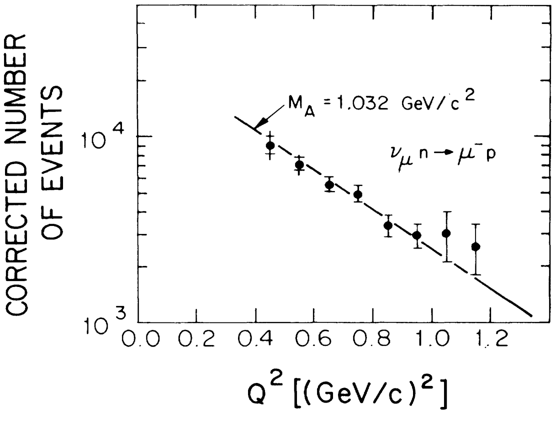

FIG. 32. The flux-averaged differential cross section for quasielastic events as measured using two-prong data (see Sec. V B). The error bars represent data events with statistical and Q^2-dependent systematic errors. The smooth curve represents the theoretical flux-averaged cross section with $M_A = 1.032$ GeV/c^2. Since no independent means of measuring the neutrino flux exists, the normalization scale on the data is arbitrary. The relative scale has been set by fixing the data normalization to the theoretical cross section.

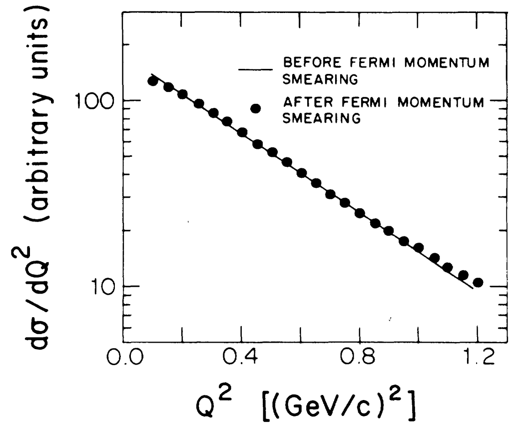

FIG. 33. The neutrino-proton elastic-scattering differential cross section with and without Fermi-momentum smearing. A 3% scale shift in the smeared distribution has been made to illustrate the consistency of the distribution shapes.

The final $\sin^2\theta_W$ values were extracted by directly fitting the final cross sections as described in Sec. VI B, and also by fitting the $\nu_\mu p$ ($\bar{\nu}_\mu p$) data and Monte Carlo—calculated Q^2 distributions to each other before acceptance corrections. This latter procedure bypasses the

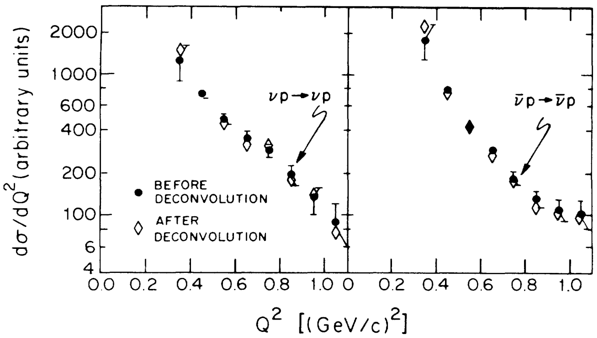

FIG. 34. The acceptance-corrected Q^2 distribution before and after resolution deconvolution. The error bars correspond to the statistical errors on the Q^2 distribution before resolution deconvolution. The neutrino and antineutrino results have been independently scaled and presented in arbitrary units.

resolution-unfolding problem by fitting resolution smeared quantities in data and Monte Carlo distributions. The results from the two procedures were nearly identical.

VI. RESULTS AND CONCLUSIONS

A. Differential cross sections

The data in Tables II and IV yield the absolute differential cross sections $d\sigma(\nu_\mu p)/dQ^2$ and $d\sigma(\bar{\nu}_\mu p)/dQ^2$ shown in Fig. 35 and Table X. The error bars in the figure and table represent statistical errors plus systematic errors of 18% and 8% on the points at $Q^2=0.45$ and 0.55 $(\mathrm{GeV}/c)^2$, respectively. Additionally, there are scale uncertainties in the $d\sigma(\nu_\mu p)/dQ^2$ and $d\sigma(\bar{\nu}_\mu p)/dQ^2$ measurements of 11.2% and 10.4% for the ν_μ and $\bar{\nu}_\mu$ results, respectively.

From the differential cross sections in Fig. 35 and the known quasielastic differential cross sections one finds the ratios[30] in the Q^2 interval $0.5 < Q^2 < 1.0$ $(\mathrm{GeV}/c)^2$:

$$R_\nu = \frac{\sigma(\nu_\mu p \to \nu_\mu p)}{\sigma(\nu_\mu n \to \mu^- p)} = 0.153 \pm 0.007(\mathrm{stat}) \pm 0.017(\mathrm{syst}) ,$$

$$R_{\bar{\nu}} = \frac{\sigma(\bar{\nu}_\mu p \to \bar{\nu}_\mu p)}{\sigma(\bar{\nu}_\mu p \to \mu^+ n)} = 0.218 \pm 0.012(\mathrm{stat}) \pm 0.023(\mathrm{syst}) ,$$

where the 11% systematic uncertainty in R_ν and $R_{\bar{\nu}}$ follows from the absolute scale uncertainty of Fig. 35 and Table X.

R_ν and $R_{\bar{\nu}}$ have been calculated over the limited interval $0.5 < Q^2 < 1.0$ $(\mathrm{GeV}/c)^2$ to reduce the overall errors in R_ν and $R_{\bar{\nu}}$ and the quantities derived from them. Some of the uncertainties in the experimental and theoretical quantities in Table VIII correlate when treating ν_μ and $\bar{\nu}_\mu$ simultaneously, which results in a smaller systematic uncertainty in quantities extracted from the combined ν_μ and $\bar{\nu}_\mu$ data.

B. Fitting procedure

To extract the best value of $\sin^2\theta_W$ and to study the axial-vector form factor, fits to the elastic-scattering differential cross sections were performed. The theoretical flux-averaged cross section in the ith Q^2 bin $(Q_i^2 < Q^2 < Q_{i+1}^2)$ is

$$\sigma_i^{\mathrm{th}} = \int_{0.2\ \mathrm{GeV}}^{5\ \mathrm{GeV}} \int_{Q_i^2}^{Q_{i+1}^2} \frac{d\sigma_{\nu p}}{dQ^2}(E_\nu, Q^2) \times \phi_\nu(E_\nu) dQ^2 dE_\nu , \qquad (6.1)$$

where $d\sigma_{\nu p}(E_\nu,Q^2)/dQ^2$ is given in Sec. I B and $\phi_\nu(E_\nu)$ is the neutrino energy spectrum. The energy interval was chosen to eliminate regions of negligible experimental acceptance. Modification of this interval caused no change in the final results.

The experimental flux-averaged cross section in the ith Q^2 bin is

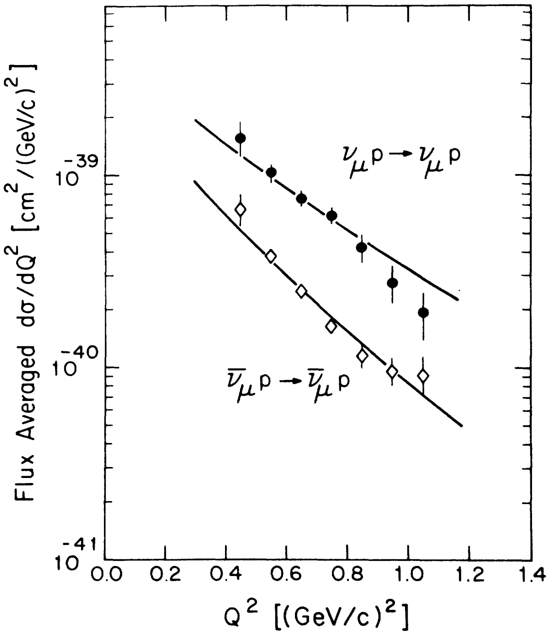

FIG. 35. The data points are the measured flux-averaged differential cross sections for $\nu_\mu p \to \nu_\mu p$ and $\bar{\nu}_\mu p \to \bar{\nu}_\mu p$ from this experiment. The solid curves are best fits to the combined data with the values $M_A = 1.06$ GeV/c^2 and $\sin^2\theta_W = 0.220$. This fitting procedure imposes adjustment of the solid curves by scale factors of 1.05 for $\nu_\mu p$ and 1.09 for $\bar{\nu}_\mu p$ consistent with the absolute scale uncertainty of approximately 11% in each of the individual cross sections which was included in the fitting procedure. The error bars represent statistical error and also include Q^2-dependent systematic errors (see Table IX).

TABLE X. Differential cross section. (The errors are statistical only. The cross sections are in cm²/GeV².)

Q^2	$d\sigma^{\nu p}/dQ^2$	$d\sigma^{\bar{\nu} p}/dQ^2$
0.45	$(0.165\pm0.011)\times10^{-38}$	$(0.756\pm0.048)\times10^{-39}$
0.55	$(0.109\pm0.008)\times10^{-38}$	$(0.426\pm0.026)\times10^{-39}$
0.65	$(0.803\pm0.076)\times10^{-39}$	$(0.283\pm0.021)\times10^{-39}$
0.75	$(0.657\pm0.064)\times10^{-39}$	$(0.184\pm0.019)\times10^{-39}$
0.85	$(0.447\pm0.073)\times10^{-39}$	$(0.129\pm0.018)\times10^{-39}$
0.95	$(0.294\pm0.064)\times10^{-39}$	$(0.108\pm0.018)\times10^{-39}$
1.05	$(0.205\pm0.057)\times10^{-39}$	$(0.101\pm0.024)\times10^{-39}$

$$\sigma_i^{\text{meas}}=\frac{N^{\nu p}}{N^{\text{QE}}}\left[\frac{\sigma_i^{\text{sig}}(\nu p)A_i^{\text{sig}}(\nu p)}{A_i^{\text{sig}}(\nu p)\left[\sigma_i^{\text{sig}}(\nu p)A_i^{\text{sig}}(\nu p)+\sum_j s_{ij}^{\text{bkgnd}}(\nu p)A_{ij}^{bkgnd}(\nu p)\right]}\right]\left[\sigma^{\text{sig}}(\text{QE})+\sum_k \sigma_k^{\text{bkgnd}}(\text{QE})A_k^{\text{bkgnd}}(\text{QE})\right] , \quad (6.2)$$

where $N_i^{\nu p}$ is the number of νp events in the ith Q^2 bin before Monte Carlo background subtraction. Similarly N^{QE} is the number of quasielastic events before Monte Carlo background subtraction. The first expression in large parentheses represents the signal acceptance and background subtraction which have been calculated by the Monte Carlo method. Here $\sigma_{ik}^{\text{bkgnd}}(\nu p)$ and $A_{ik}^{\text{bkgnd}}(\nu p)$ represent the cross sections and acceptance for all νp backgrounds in the ith Q^2 bin. The last expression in large parentheses contains acceptance and background factors for the observed quasielastic events. The flux-averaged cross sections and acceptances for the quasielastic and elastic samples are defined identically.

The fits were carried out using the computer program MINUIT (Ref. 31). The χ^2 minimized was

$$\chi^2=\sum_{ij}(\sigma_i^{\text{th}}-\sigma_i^{\text{meas}})E_{ij}{}^{-1}(\sigma_j^{\text{th}}-\sigma_j^{\text{meas}}) , \quad (6.3)$$

where E_{ij} is the full correlated error matrix including statistical errors as well as Q^2-dependent and correlated Q^2-independent errors. In performing the fit, $\sin^2\theta_W$ and the axial-vector form factor dependences have been taken into account in the acceptance, background subtraction, and normalization factors in Eq. (6.2). These factors slightly lower the fit sensitivity.

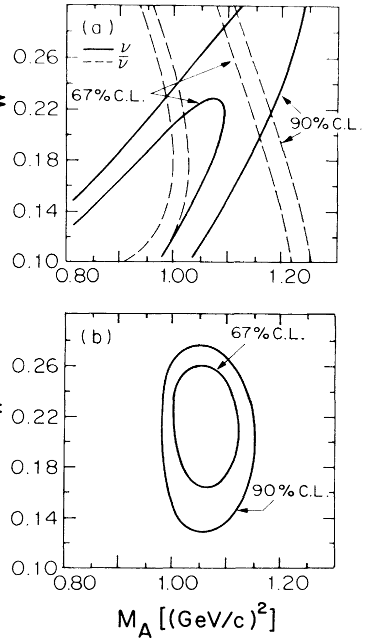

FIG. 36. Final-fit confidence-level contours in $\sin^2\theta_W$, M_A space for (a) $d\sigma/dQ^2$ fit individually for the neutrino and antineutrino elastic-scattering samples. Note the relative insensitivity to $\sin^2\theta_W$ for the antineutrinos. (b) A simultaneous fit to both neutrino and antineutrino differential cross sections.

C. Results

To extract values of the axial-vector mass M_A and $\sin^2\theta_W$, corrections to the axial-vector form factor were taken to be zero initially [$\eta=0$ in Eq. (1.13)]. The cross sections $d\sigma(\nu_\mu p)/dQ^2$ and $d\sigma(\bar{\nu}_\mu p)/dQ^2$ were fit over the interval $0.4<Q^2<1.1$ $(\text{GeV}/c)^2$. In Fig. 36 are plotted the 67% and 90%-confidence-level boundaries on $\sin^2\theta_W$ and M_A for (a) individual fits to $d\sigma(\nu_\mu p)/dQ^2$ and $d\sigma(\bar{\nu}_\mu p)/dQ^2$, and (b) for a simultaneous fit to both. It is seen that the differential cross section for $\nu_\mu p$ is sensitive to both M_A and $\sin^2\theta_W$ while the differential cross section for $\bar{\nu}_\mu p$ is sensitive primarily to M_A.

The simultaneous fit to both $d\sigma(\nu_\mu p)/dQ^2$ and $d\sigma(\bar{\nu}_\mu p)/dQ^2$ yields

$$\begin{aligned}\sin^2\theta_W&=0.218^{+0.039}_{-0.047} ,\\ M_A&=1.06\pm0.05 \text{ GeV}/c^2 ,\end{aligned} \quad (6.4)$$

where the errors represent a 67% rectangular confidence area. The χ^2 for this fit is 15.8/14 DF. These best-fit curves are also displayed on the differential cross section plots of Fig. 35. This value of M_A is in good agreement with the present world-average value: $M_A=1.032\pm0.036$ GeV/c^2.

To search for additional terms in the axial-vector current $G_A(Q^2)$ is parametrized as in Eq. (1.13). Fixing $\sin^2\theta_W$ at 0.22 and constraining M_A to the world-average value, a simultaneous fit to $d\sigma(\nu_\mu p)/dQ^2$ and $d\sigma(\bar{\nu}_\mu p)/dQ^2$ was performed. The result is $\eta=0.12\pm0.07$ or equivalently, $0.00<\eta<0.25$ at 90% C.L. This result for η is independent of the numerical value assumed for $\sin^2\theta_W$.

The possibility of a positive η term clouds the axial-vector mass measurement derived from the neutral-

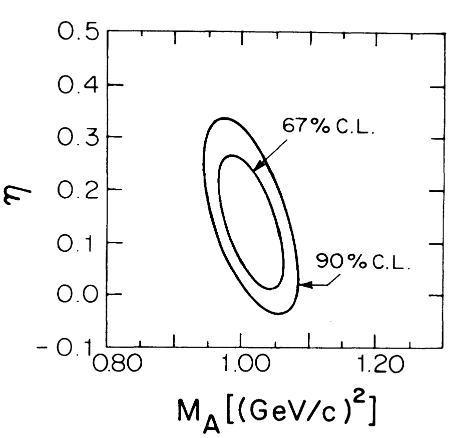

FIG. 37. Simultaneous fit of $d\sigma/dQ^2$ for the neutrino and antineutrino elastic-scattering samples in M_A,η space with $\sin^2\theta_W$ fixed at 0.220. M_A has been constrained to the world-average value.

TABLE XI. Values of $\sin^2\theta_W$ obtained from the combined ν_μ and $\bar{\nu}_\mu$ data with the axial-vector isovector form factor mass constrained to be $M_A = 1.032 \pm 0.036$ GeV. The first error given is the statistical error. The second error corresponds to the systematic error on the result.

Measured quantities	$\sin^2\theta_W$		χ^2/DF
R_ν and $R_{\bar{\nu}}$	0.207 ± 0.016	$+0.032$ -0.048	1.1/1
$\sigma(\bar{\nu}_\mu p \to \bar{\nu}_\mu p)/\sigma(\nu_\mu p \to \nu_\mu p)$[a]	0.228 ± 0.016	$+0.028$ -0.037	0.0/0
$d\sigma(\nu_\mu p)/dQ^2$ and $d\sigma(\bar{\nu}_\mu p)/dQ^2$	0.220 ± 0.016	$+0.023$ -0.031	16/15

[a] $\sigma(\bar{\nu}_\mu p \to \bar{\nu}_\mu p)/\sigma(\nu_\mu p \to \nu_\mu p)$ is given by

$$\frac{R_{\bar{\nu}} \int_{0.5}^{1.0} [d\sigma(\bar{\nu}_\mu p \to \bar{\nu}_\mu p)/dQ^2] dQ^2}{R_\nu \int_{0.5}^{1.0} [d\sigma(\nu_\mu p \to \nu_\mu p)/dQ^2] dQ^2} = 0.302 \pm 0.019 \pm 0.037 \; .$$

current data. Shown in Fig. 37 are 90%-C.L. bounds on M_A and η. Here a simultaneous fit to $d\sigma(\nu_\mu p)/dQ^2$ and $d\sigma(\bar{\nu}_\mu p)/dQ^2$ has been performed with $\sin^2\theta_W$ fixed at 0.220. It is seen that η and M_A are strongly correlated.

The quantity η may be as due either to (1) heavy-quark currents, or (2) a "nonstandard" axial-vector isovector term. Several attempts have been made to estimate the heavy-quark current portion of this term. Collins, Wilczek, and Zee[17] have estimated $\eta = 0.04$ from the diagram in which two gluons are exchanged between a heavy-quark loop and a valence quark. Wolfenstein[17] has estimated $\eta = 0.10 \pm 0.15$. The experimental result is therefore in agreement with expectation.

To exhibit the internal consistency of the data, and to extract the most precise value of $\sin^2\theta_W$, M_A was constrained at the world-average value and $\sin^2\theta_W$ was calculated in all ways that combine the ν_μ and $\bar{\nu}_\mu$ data. The resulting three values are shown in Table XI. The extracted values of $\sin^2\theta_W$ are insensitive to any choice of η in the region of $0.0 < \eta < 0.25$ as is shown in Fig. 38. Taking into account the increased information in the differential cross sections, the most precise value of $\sin^2\theta_W$ from this measurement is

$$\sin^2\theta_W = 0.220 \pm 0.016(\text{stat})^{+0.023}_{-0.031}(\text{syst}) \; . \tag{6.5}$$

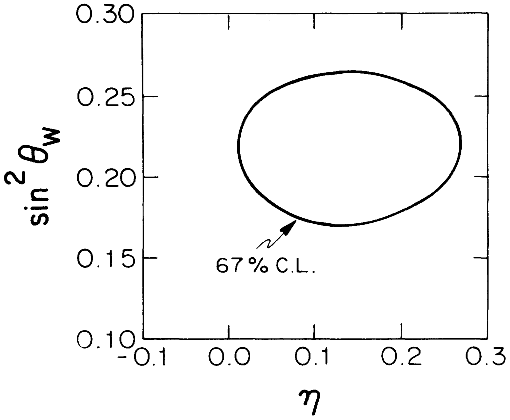

FIG. 38. Simultaneous fit of $d\sigma/dQ^2$ for the neutrino and antineutrino elastic-scattering samples in $\sin^2\theta_W,\eta$ space with M_A separately minimized at each point. M_A has been constrained to the world-average value. The insensitivity of $\sin^2\theta_W$ to the value of η is clearly demonstrated.

D. Summary and conclusion

We have reported new measurements of R_ν, $R_{\bar{\nu}}$, $d\sigma_\nu/dQ^2$, and $d\sigma_{\bar{\nu}}/dQ^2$ for neutrino-proton and antineutrino-proton elastic scattering. The cross sections are consistent with the standard model SU(2)×U(1). The data suggest the possibility of an additional term to the axial-vector form factor $G_A(Q^2)$ at 90% C.L., which may be due to (1) heavy-quark currents, or (2) a "nonstandard" axial-vector isoscalar current. The data yield a measurement of $\sin^2\theta_W$:

$$\sin^2\theta_W = 0.220 \pm 0.016(\text{stat})^{+0.023}_{-0.031}(\text{syst}) \; . \tag{6.6}$$

In an earlier paper[32] we reported a value of

$$\sin^2\theta_W = 0.209 \pm 0.029(\text{stat}) \pm 0.013(\text{syst}) \; ,$$

obtained from measurements of the cross sections for the purely leptonic reactions $\nu_\mu e \to \nu_\mu e$ and $\bar{\nu}_\mu e \to \bar{\nu}_\mu e$ with the same apparatus and using the identical normalization procedure as the present analysis. There is good agreement between this value and the value obtained from the $\nu_\mu p$ and $\bar{\nu}_\mu p$ cross sections.

Table XII displays the central values of $\sin^2\theta_W$ with as-

TABLE XII. Experimental measurements of $\sin^2\theta_W$.

Reaction	Typical Q^2 (GeV)	$\sin^2\theta_W$ ($\rho = 1$)
W,Z	10^4	0.224 ± 0.007
$e^+e^- \to \mu^+\mu^-$	10^3	0.17 ± 0.02
Deep inelastic	10^2–10^3	0.226 ± 0.008
μC asymmetry	10^2	0.24 ± 0.08
$\nu p \to \nu p$	10^0	0.22 ± 0.03
eD asymmetry	10^0	0.220 ± 0.014
$\nu e \to \nu e$	10^{-2}	0.23 ± 0.02
Atomic parity	10^{-11}	0.19 ± 0.04

sociated errors obtained from fits to the world samples of measurements of the weak neutral current[33] by different experimental techniques. The results cover a Q^2 range from 10^4 to 10^{-11} $(\text{GeV}/c)^2$. It is seen that the result of this experiment is in good agreement with all other measurements of $\sin^2\theta_W$. Within present experimental errors of about 10% the weak-neutral-current parameter $\sin^2\theta_W$ is a universal constant.

ACKNOWLEDGMENTS

We are grateful to W. J. Marciano for discussions of the radiative corrections and to Paul Langacker for many informative discussions. We wish to thank R. R. Rau and N. P. Samios of Brookhaven National Laboratory for their encouragement and the staff of the AGS for providing the high-quantity beam. We also wish to thank the technical assistance personnel at the respective institutions, for their excellent and untiring support. This work was supported in part by the U.S. Department of Energy, the Japanese Ministry of Education, Science and Culture through the Japan-U.S.A. Cooperative Research Project on High Energy Physics.

APPENDIX

Monte Carlo calculation: general

A Monte Carlo program[24] was developed to determine background fractions and acceptances of the signal and normalization samples, as well as to study sensitivity to various cuts in the analysis. The program generated events in all the signal and background channels of interest using the measured neutrino fluxes and theoretical differential cross sections. It transported particles through a model of the detector incorporating detector geometry and properties of the detector materials. Output of the Monte Carlo program was subjected to analysis identical to that of the signal and normalization samples.

Particle generation

Events were generated with energy distributions determined by the measured neutrino fluxes.[19] The transverse neutrino beam profile was determined by a beam Monte Carlo method, and the z dependence by the solid-angle acceptance of the detector.

Assignment of the target nucleus was made according to the known distribution of materials in the detector and their chemical composition. For reactions on nucleons in complex nuclei, the target nucleon was given an initial momentum distributed according to momentum distributions measured in nuclei by electron scattering.[28] Where appropriate, a shell-model calculation suppressed low-Q^2 events.[35]

Neutrino interactions with bound nucleons involved additional complexity due to the high probability of the outgoing nucleon to interact with the surrounding nuclear material in the same nucleus, thus liberating additional particles which could mask the signature of a given final state. The probability of a rescatter was determined from nucleon-nucleon cross sections and the nucleon density (modeled with harmonic-oscillator wave functions[36]) integrated along the path of the escaping nucleon. If a particle was determined to have scattered, one of several nucleon-nucleon scattering reactions was calculated. The recoil particle in a rescattering interaction was assigned a 50% probability of undergoing a further scatter. This probability was tuned to match the frequency and multiplicity distribution of secondary particles observed in bubble-chamber neutrino interactions.[23,37,38]

Particle transport

Each particle was stepped through the detector in small segments; the ionization loss[39] per segment was subtracted from the kinetic energy, and the particle direction modified to account for multiple scattering[40] in the segment. Particles were transported until they stopped, excited the detector, decayed, or changed flavor in an interaction. Stopping pions were absorbed in nuclei causing a nuclear breakup.

Nucleon scattering took into account elastic and inelastic reactions. The detailed scattering mechanism was determined from the relative probabilities of (1) elastic scattering on a free proton, (2) inelastic scattering on a free proton, (3) elastic scattering in a carbon nucleus, and (4) inelastic scattering in a carbon nucleus.[41–44] The latter interactions were treated in a quasifree approximation and handled similarly to interactions with single nucleons.

Pion scattering was treated similarly. In addition to pion-nucleon scattering, pion reactions included the possibility of pion absorption in a nucleus and charge exchange. Charged pion-nucleon elastic scattering, and pion-nucleon charge exchange were specified by the appropriate differential and total inelastic cross sections.[45,46] The inelastic scattering model allowed for final states involving a π^0 with charge exchange of the initial-state particles fixed by isospin invariance. The kinematics of these reactions were thrown uniformly in three-body phase space.

Output

The final phase of the Monte Carlo calculation converted ionization losses into energy deposits within detector elements along with time of passage. The detector energy response included saturation and threshold effects to bring the observed energy and time resolution in agreement with test beam measurements.[18] The output of the Monte Carlo program was processed through the identical analysis code used to extract the data signal (see Sec. III). This assured that similar fiducial, PID, and analysis cuts were applied to both data and Monte Carlo events. In analyzing Monte Carlo events, real data were overlaid on Monte Carlo events to ensure that random noise and event overlap were properly evaluated.

[*] Deceased.

[†] Permanent address: Singer Co., Kearfott Div., Wayne, NJ 07470.

[‡] Now at KEK.

[§] Now at Los Alamos National Laboratory, Los Alamos, NM 87544.

[**] Now at Sumitomo Heavy Industry, Tokyo, Japan.

[††] Permanent address: Christopher Newport College, Department of Physics, Newport News, VA 23606.

[‡‡] Permanent address: M.I.T. Lincoln Laboratory, Lexington, MA 02173.

[§§] Permanent address: Cornell University, Department of Physics, Ithaca, NY 14853.

[1] G. Barbiellini and C. Santoni, Riv. Nuovo Cimento **9**, 2 (1985); M. Klein, Fortschr. Phys. **33**, 375 (1985); L. M. Sehgal, in *Neutral Currents, Theory and Application, Progress in Particle and Nuclear Physics,* edited by A. Faessler (Pergamon, New York, 1985), Vol. 14, p. 1.

[2] S. Glashow, Nucl. Phys. **22**, 579 (1961); S. Weinberg, Phys. Rev. Lett. **19**, 1264 (1967); A. Salam, in *Elementary Particle Theory,* edited by N. Svartholm (Almqvist & Wiksell, Stockholm, 1968), p. 367.

[3] UA1 Collaboration, T. Arnison *et al.*, Phys. Lett. **129B**, 273 (1983); UA2 Collaboration, P. Bagnaia *et al.*, *ibid.* **129B**, 130 (1983).

[4] Paul Langacker, Comments Nucl. Part. Phys. **XV**, 41 (1985).

[5] W. Marciano (private communication).

[6] W. Lee *et al.*, Phys. Rev. Lett. **37**, 186 (1976).

[7] D. Cline *et al.*, Phys. Rev. Lett. **37**, 262 (1976).

[8] M. Pohl *et al.*, Phys. Lett. **72B**, 448 (1978).

[9] H. Faissner *et al.*, Phys. Rev. D **21**, 555 (1980).

[10] D. Coteus *et al.*, Phys. Rev. D **24**, 1420 (1981); D. Cline *et al.*, Phys. Rev. Lett. **37**, 648 (1976).

[11] J. Horskotte *et al.*, Phys. Rev. D **25**, 2743 (1982).

[12] K. Abe *et al.*, Phys. Rev. Lett. **56**, 1107 (1986).

[13] We have followed the formulas of E. Fischbach *et al.*, Phys. Rev. Lett. **37**, 582 (1976); Phys. Rev. D **15**, 97 (1977); J. Kim *et al.*, *ibid.* **18**, 123 (1978); Rev. Mod. Phys. **53**, 211 (1981).

[14] M. Olsson *et al.* Phys. Rev. D **17**, 2938 (1978); B. Bartoli *et al.*, Riv. Nuovo Cimento **2**, 2411 (1972).

[15] J. Kim *et al.*, Rev. Mod. Phys. **53**, 211 (1981).

[16] N. Baker *et al.*, Phys. Rev. D **23**, 2499 (1981); K. Miller *et al.*, *ibid.* **26**, 537 (1982); T. Kitagaki *et al.*, *ibid.* **28**, 436 (1983).

[17] J. Collins *et al.*, Phys. Rev. D **18**, 242 (1981); R. Mohapatra *et al.*, *ibid.* **19**, 2165 (1979); S. Oneda *et al.*, Phys. Lett. **88B**, 343 (1979); L. Wolfeinstein, Carnegie-Mellon University Report No. C00-3066-119, 1979 (unpublished).

[18] L. A. Ahrens *et al.* Nucl. Instrum. Methods (to be published).

[19] L. A. Ahrens *et al.*, Phys. Rev. D **34**, 75 (1986).

[20] D. Doughty, University of Pennsylvania, Ph.D. thesis, 1984.

[21] Energy loss in scintillator, Lucite, and aluminum is taken from W. Barkus and M. Berger, Report No. NASA SP-3013, 1964 (unpublished). Energy loss in the PDT gas is taken from R. M. Sternheimer and R. F. Peierls, Phys. Rev. B **3**, 3681 (1971).

[22] D. Rein and L. Sehgal, Ann. Phys. (N.Y.) **133**, 79 (1981).

[23] G. S. Ormazabal, Report No. Nevis-251, 1985 (unpublished).

[24] E. Stern, Ph.D. thesis, S.U.N.Y. Stony Brook, 1986.

[25] The measured value of R_{ν} from the alternate analysis was 0.140±0.008(stat) compared to 0.153 and of $R_{\bar{\nu}}$ was 0.223±0.015(stat) compared to 0.218.

[26] C. H. Llewellyn-Smith, Phys. Rep. **3C**, 261 (1972); R. M. Barnett, Phys. Rev. D **15**, 97 (1977).

[27] Particle Data Group, O. Benary and L. Price, Report No. UCRL-20000NN, 1970 (unpublished).

[28] Information pertaining to nucleon binding energy and momentum distributions in carbon was obtained from J. Mougey *et al.*, Nucl. Phys. **A262**, 461 (1976). Additional information concerning nucleon momentum distributions in carbon was taken from A. Bodek and J. L. Ritchie, Phys. Rev D **23**, 1070 (1981).

[29] See, for example, W. Krenz *et al.*, Nucl. Phys. **B135**, 45 (1978); N. Baker *et al.*, Phys. Rev. D **23**, 2495 (1981).

[30] The value for the statistical error on $R_{\bar{\nu}}$ was incorrectly quoted at 0.008 in the earlier report given in Ref. 12.

[31] F. James and M. Roos, Comput. Phys. Commun. **10**, 343 (1975).

[32] L. Ahrens *et al.*, Phys. Rev. **54**, 18 (1985).

[33] U. Amaldi *et al.* (unpublished).

[34] For neutrino-baryon elastic scattering the cross sections used were discussed in Sec. I. For quasielastic scattering cross sections see Ref. 26. For single-pion-production cross sections see Ref. 22.

[35] J. S. Bell and C. H. Llewellyn Smith, Nucl. Phys. **B28**, 317 (1971).

[36] At. Data Nucl. Data Tables, **14**, No. 5, (1974); **14**, No. 6, (1974).

[37] E. Fett *et al.*, Nucl. Instrum. Methods **144**, 109 (1977).

[38] R. L. Ford, and W. R. Nelson, SLAC Report No. 210, 1978.

[39] For liquid scintillator, the formulas developed in B. Rossi, *High Energy Particles* (Prentice-Hall, New York, 1952), p. 32 were used. For ionization in PDT gas, density effects become important. The formulation for the peak energy loss used is given in R. M. Sternheimer and R. F. Peierls, Phys. Rev. B **3**, 3681 (1971). The width of the distributions was parametrized from the data and calculations reported in Harris *et al.*, Nucl. Instrum. Methods **107**, 413 (1973); K. Isparian *et al.*, *ibid.* **117**, 125 (1974); V. C. Ermilova *et al.*, *ibid.* **145**, 555 (1977).

[40] J. B. Marion and B. A. Zimmerman, Nucl. Instrum. Methods **51**, 93 (1967); J. L. Highland, *ibid.* **129**, 497 (1975).

[41] M. Eckhause *et al.*, Nucl. Phys. **81**, 575 (1966).

[42] E. Bellotti, D. Cavalli, and C. Matteuzzi, Nuovo Cimento **18A**, 75 (1973).

[43] For *pn* and *pp*, Particle Data Group, Rev. Mod. Phys. **52**, S1 (1980); for proton-carbon, R. E. Richardson *et al.*, Phys. Rev. **86**, 29 (1952); for neutron-carbon, T. B. Taylor, *ibid.* **92**, 831 (1953).

[44] J. P. Auger and R. J. Lombard, Phys. Lett. **45B**, 115 (1973).

[45] Lock and Measday, *Intermediate Energy Nuclear Physics, 62* (Metheuen, London, 1970).

[46] J. Hüfner, Phys. Rep. **21**, No. 1 (1975); J. W. Cronin *et al.*, Phys. Rev. **107**, 1121 (1957); M. Crozon *et al.*, Nucl. Phys. **64**, 567 (1965); D. Ashery *et al.*, Phys. Rev. Lett. **42**, 1465 (1979); P. U. Renberg *et al.*, Nucl. Phys. **A183**, 81 (1972).